ADVANCED MATERIALS TECHNOLOGIES
www.advmattechnol.de

Herringbone Microfluidic Probe for Multiplexed Affinity-Capture of Prostate Circulating Tumor Cells

*Ayoub Glia, Muhammedin Deliorman, Pavithra Sukumar, Farhad K. Janahi, Bisan Samara, Ayoola T. Brimmo, and Mohammad A. Qasaimeh**

In this work, for first time, circulating tumor cells (CTCs) are captured on an open biofunctionalized substrate with multiplexing capability. This is achieved by developing a new microfluidic probe (MFP) integrated with radially staggered herringbone (HB) elements for microvortex generation. The new tool, named as herringbone microfluidic probe (HB-MFP), is a channel-less microfluidic system with physically separated bottom capture substrate and top fluidics delivery system. The concept allows for functionalizing the capture substrate with multiple biorecognition ligands (in this work, stripes of different capture antibodies) and scanning the fluidics delivery system across the substrate in a 2D printing-like movement. Using the HB-MFP, CTCs are efficiently captured from prostate cancer blood samples through their specific EpCAM, PSMA, and PSA antigens in a single run, with counts ranging from as low as 6 CTCs mL^{-1} (localized cancer patients) to as high as 280 CTCs mL^{-1} (metastatic cancer patients). In the process, CTC clusters with sizes of as high as 40–50 cells are also successfully captured. The results indicate that multiplex profiles of CTCs could reveal certain cellular phenotypes based on PSMA and PSA expression levels. The developed HB-MFP is simple and robust to use, allows for high throughput sample processing, and provides seamless access to captured CTCs for further downstream characterization.

1. Introduction

Prostate cancer is one of the most prevalent and life-threatening cancers among men.[1] As in any other cancer, metastasis in prostate cancer initiates the pathway to fatality.[2] In particular, when cancer spreads to bones, the five-year survival rate of patients with localized stage is reduced from 78% to 5%.[1,3] Clearly, the detection of prostate cancer at the earliest curable stage is paramount for preventing its spread by means of implemented treatment strategies.[4]

Performing direct rectal examination (DRE) and measuring prostate-specific antigen (PSA) serum levels are the two standards for early cancer detection.[5] However, these procedures are generally plagued with several uncertainties. For instance, in the case of DRE, neither the presence nor the absence of abnormalities in prostate gland (based on the doctor feeling) can ascertain an accurate diagnostic profile.[6] That is, the tumor might present characteristics similar to normal tissue, normal tissue might exhibit abnormalities of tumor, or tumor could be in unreachable location in the prostate gland. In addition to the fact that patients are reluctant to undergo the exam,[7] reports also suggest that DRE is less sensitive than a PSA test.[8,9] On the other hand, false positives and negatives in PSA serum levels are generally responsible for erroneous detection in prostate cancer.[10,11] As a result, the inaccuracies in DRE and PSA screening induce psychological trauma in patients and, in many cases, lead to unnecessary invasive tissue biopsies.[9]

To minimize the negative effects on patients and uncertainties related to diagnostic accuracy, there has been a growing motivation toward developing less invasive liquid biopsy approaches,[12] where technological miniaturizations require small sample volumes and offer high precision, thus achieving higher sensitivity at lower cost.[13] One of the main targets in liquid biopsies is circulating tumor cells (CTCs), the malignant cells that detach from main tumor and enter to and disseminate within the bloodstream at early stage of tumorigenesis.[2] Thus, the presence of CTCs in blood could constitute a prognostic marker for cancer metastasis, providing that their capture and identification occur in a timely manner.[14] However, the scarcity of these cells in blood (≈–1000 per mL in the midst

A. Glia, Dr. M. Deliorman, P. Sukumar, B. Samara, Dr. A. T. Brimmo, Prof. M. A. Qasaimeh
Division of Engineering
New York University Abu Dhabi (NYUAD)
P.O. Box 129188, Abu Dhabi, UAE
E-mail: mohammad.qasaimeh@nyu.edu
A. Glia, Dr. A. T. Brimmo, Prof. M. A. Qasaimeh
Department of Mechanical and Aerospace Engineering
New York University
Brooklyn, NY 11201, USA
Dr. F. K. Janahi
College of Medicine
Mohammed Bin Rashid University of Medicine and Health Sciences
P.O. Box 505055, Dubai, UAE
The ORCID identification number(s) for the author(s) of this article can be found under https://doi.org/10.1002/admt.202100053.

DOI: 10.1002/admt.202100053

of millions of white blood cells and billions of red blood cells) makes their isolation extremely challenging.

With the advent of microfluidics, processing small amount of blood samples has become well suited for the isolation of CTCs. As a result, using various microfluidic chip designs, CTCs were successfully isolated from blood of cancer patients based on their sizes,[15] mechanical properties,[16] dielectric properties,[17] and surface antigens.[18] In the latter, the capture is more targeted and specific to cancer type, since the surface antigens of CTCs are known to serve as biomarkers in their identification.[19] Hence, many of the typical "closed-channel" microfluidic devices for CTC capture, pioneered by the Herringbone-Chip (HB-Chip),[20] rely on herringbone elements for laminar blood mixing to enhance the capture of CTCs through ligand–receptor interactions.[21] However, existing challenges with these approaches mainly stem from associated high shear stresses within the narrow channels and restricted access to captured CTCs for downstream analysis.[22] In addition, common to these devices is the monoplexed cell capture, which limits the simultaneous use of multiple bio-recognition ligands.[23] The Biocept platform[24] is an exception to this category, wherein a cocktail of multiple recognition molecules is deployed for cell capture. However, the platform does not provide the knowledgebase of the specific recognition molecules responsible for the cell capture. Furthermore, most microfluidic devices are designed to isolate single CTCs and not CTC clusters, a limitation that exists due to high shear stresses and clogging within narrow channels. Recently developed technologies, such as MCI[25] and cluster-chip,[26] are examples with good performance on CTC cluster capture under low shear stresses. However, their performance relies on physical traps which pose a size limitation on the captured clusters, make devices susceptible to clogging, and limit multiplexed capture of CTCs.

Here, we developed an open-space microfluidic system to efficiently capture, through antibody-antigen interactions, single CTCs and CTC clusters directly from peripheral blood of prostate cancer patients. We show high throughput blood processing combined with great flexibility to multiplex functionalize the capture substrate, give full access to captured cells for post-processing steps, and provide capability to capture CTC clusters with no size restrictions. In our system-exemplified by the concept of the microfluidic probe (MFP)[27]—the probe and the substrate are fully decoupled, where the hydrodynamic flow confinement (HFC) provides "virtual walls" to confine the processed fluid.[28] The open configuration also allows easy access of cells (by simply pulling the probe away from substrate) for postcapture analysis.[29] Meanwhile, the MFP comes with ability to scan over the capture substrate in a 2D printing mode, which brings multiplexed cell capture functionality. All these are desirable features considering the heterogeneous nature of CTCs; especially when the expression of surface proteins in CTCs vary greatly with their highly adaptive characteristics.[30] Nevertheless, since their first introduction,[31] the MFPs have already been deployed in several applications, such as cell stimulation[32] and manipulation.[33,34] More recently, we have developed 3D printing methodologies to manufacture MFPs with great modular capability in the design,[35,36] thus easing the implementation of new concepts and applications with simple design adjustments.

Our rational in this study is to combine, for first time, a unique design of MFP with chaotic micromixing (using radially staggered herringbone elements), multiple specific capture antibodies, and immunocytochemistry for the isolation and subsequent identification of prostate CTCs in single and aggregate forms. With the developed HB-MFP, we demonstrate a seamless open-space microfluidic platform that provides an improved throughput and cell capture efficiency for liquid biopsy applications while avoiding problems of elevated shear stresses and clogging. To deduce the optimal operational conditions, we first investigate the key parametric features of HB-MFP. Then, using human prostate cancer cell lines (LNCaP and PC3), breast cancer cell line (MCF-7), lymphoblast T cell line (MOLT4), and lymphocyte Jurkat T (JKT) cell line, we assess the throughput, cell capture efficiency, and nonspecific binding. Finally, by using three different capture antibodies that target epithelial cell adhesion molecule (EpCAM), prostate-specific membrane antigen (PSMA) and prostate-specific antigen (PSA) of cells, we reveal multiplexed functionality in capturing CTCs (single or in form of clusters) from blood samples taken from patients with localized and metastatic prostate cancer.

2. Results

2.1. The Herringbone-Microfluidic Probe (HB-MFP)

The working principle, scanning mode operation, and experimental apparatus of the HB-MFP are illustrated in **Figure 1**a–c. The device (3D printed using stereolithography printer, see Experimental Section for details) possesses an open-space microfluidic configuration, where the probe is fully decoupled from the substrate. This allows for independent substrate handling and functionalization. A twist-lock mechanism is implemented to connect the HB-MFP to a programmable XYZ micropositioner, so that the device parallel alignment, separation distance, and scanning speed and direction are precisely controlled. This way, spatial flexibility is introduced, where large areas can be efficiently scanned, and localized areas can be easily targeted. As a result, we show that CTCs can be captured, with multiplexing, on an open flat substrate in a 2D printing configuration. The movements of HB-MFP could follow straight horizontal path or a zig-zag pattern (Figure 1b), providing that the HB-MFP thoroughly scans the substrate. Moreover, as the HB-MFP is connected to the computer-controlled XYZ micropositioner, the HB-MFP can move along any pre-designed or arbitrary path and at different given scanning speeds.

In the device (see Figure S1, Supporting Information for top, bottom, side, and sectioned side views), three fluidic tube ports are linked to two symmetrical crescent-shaped aspiration peripheral apertures facing each other and one circular injection aperture in the middle (Figure 1d). The apertures are designed to form a processing area on the capture substrate with ≈4 mm radius, which reflects the distance between aspiration and injection apertures. To achieve the HFC between the tip surface of HB-MFP (called mesa) and the substrate, the ratio of the fluid aspiration to that of injection flow rates ($\alpha = Q_{Asp}/Q_{Inj}$) is maintained above the theoretical limit (i.e., $\alpha = 1.5$ based on fluidic dipolar configuration[37]).

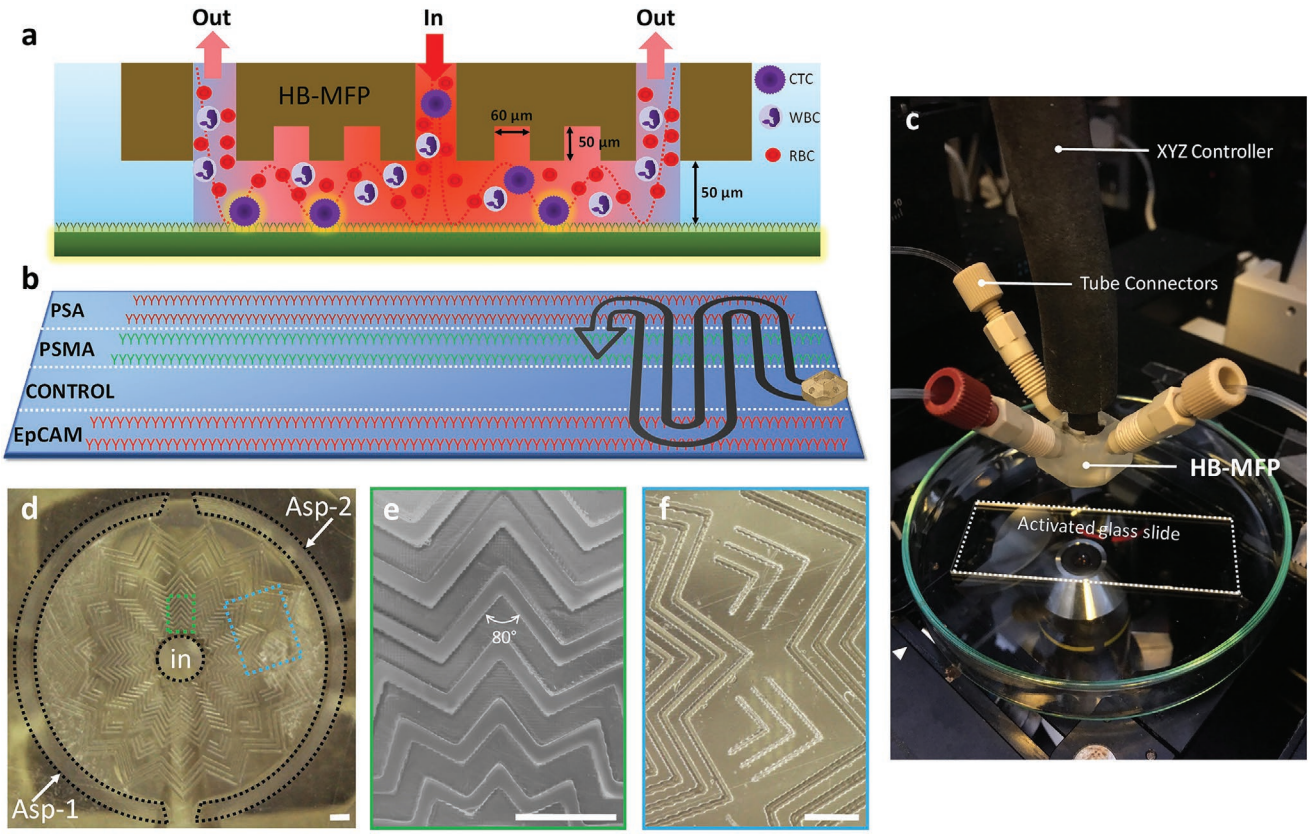

Figure 1. The herringbone-microfluidic probe (HB-MFP). a) The schematic depicts the working concept of the HB-MFP, where blood is injected from the central aperture and aspirated from the crescent-shaped peripheral apertures. The confined blood (HFC) is in purple and the staggered grooves (HB elements) are in brown. b) Schematic shows the HB-MFP hovering in a zig-zag pattern over antibody stripes against EpCAM, PSMA, and PSA capture. This provides a thorough scan of the substrate. c) Micrograph shows the experimental setup, where the HB-MFP is connected by a twist-lock mechanism to XYZ micropositioner mounted on stage of inverted microscope. d) Micrograph shows the tip surface of the 3D printed HB-MFP with the central injection aperture (in), two crescent-shaped aspiration apertures (Asp-1 and Asp-2), and radially staggered HB elements. e,f) Zoomed images of dashed boxes in (d) show the radial structure and surface finish of the HB elements. Scale bars in (d–f) are 0.5 mm.

The HB-MFP is integrated with radial micromixers for enhanced cell capture efficiency, a redesigned feature based on the well-established herringbone (HB) microvortex-generating elements.[38] As such, these elements increase the chaotic mixing of the fluid (e.g., blood), thus breaking the laminar envelope of its content. As a result, the interaction of CTCs with the capture antibodies on the substrate surface is achieved. The redesigned micromixers are implemented in radial manner across the separation distance between the two aspiration apertures (Figure 1e,f), where each is 100 µm wide, 40 µm deep, and oriented at 80° with 60 µm gaps in between them. The 80° angle in the HB structure was designed for the radial flow to experience maximum angular displacement (i.e., twisting),[38] thus optimizing cell-surface interactions. Further evaluation including finite element modeling of the optimized angle is left for future studies.

2.2. Parametric Optimization of the HB-MFP

To assess better the functionality of the device for enhanced microvortex generation while operating in the scanning mode, we carried a parametric optimization study of the HB-MFP using steady-state computational fluid dynamics simulations. Here, the preservation of HFC was taken into account when optimizing the ratio of aspiration/injection flow rates (α), scanning speeds (β), and the ratio of mesa/processing area (φ). Then, the cutoff scanning speeds (ω) were simulated for all combinations of α and φ, and the shear stresses within the HFC were calculated. This way, the key parametric values of HFC were obtained by analyzing the velocity streamlines plots and 2D flow maps within the plane of fluid processing area. **Figure 2**a illustrates the velocity streamlines of a typical HB-MFP setting, where the fluid is injected from the central aperture and entirely aspirated from the outer crescent-shaped apertures indicating the occurrence of total HFC.

One important aspect of the HB-MFP is its ability to process large volumes (>5 mL) of fluids in relatively short time frames (<2 h). Therefore, it is essential to consider the shear stresses endured by the blood streams during cell capture experiments, given that shearing plays a decisive role in obtaining high cell capture and maintaining cell integrity and viability.[23] In this regard, the effects of the scale (i.e., fluid processing area) and flow rates on the shear stresses within the HFC were examined under constant aspiration/injection flow rates (α). Hence, fluid processing areas with 2 and 4 mm radius (R) were chosen and injection flow rates of 1.2 and 3.6 mL h^{-1} were tested. In both

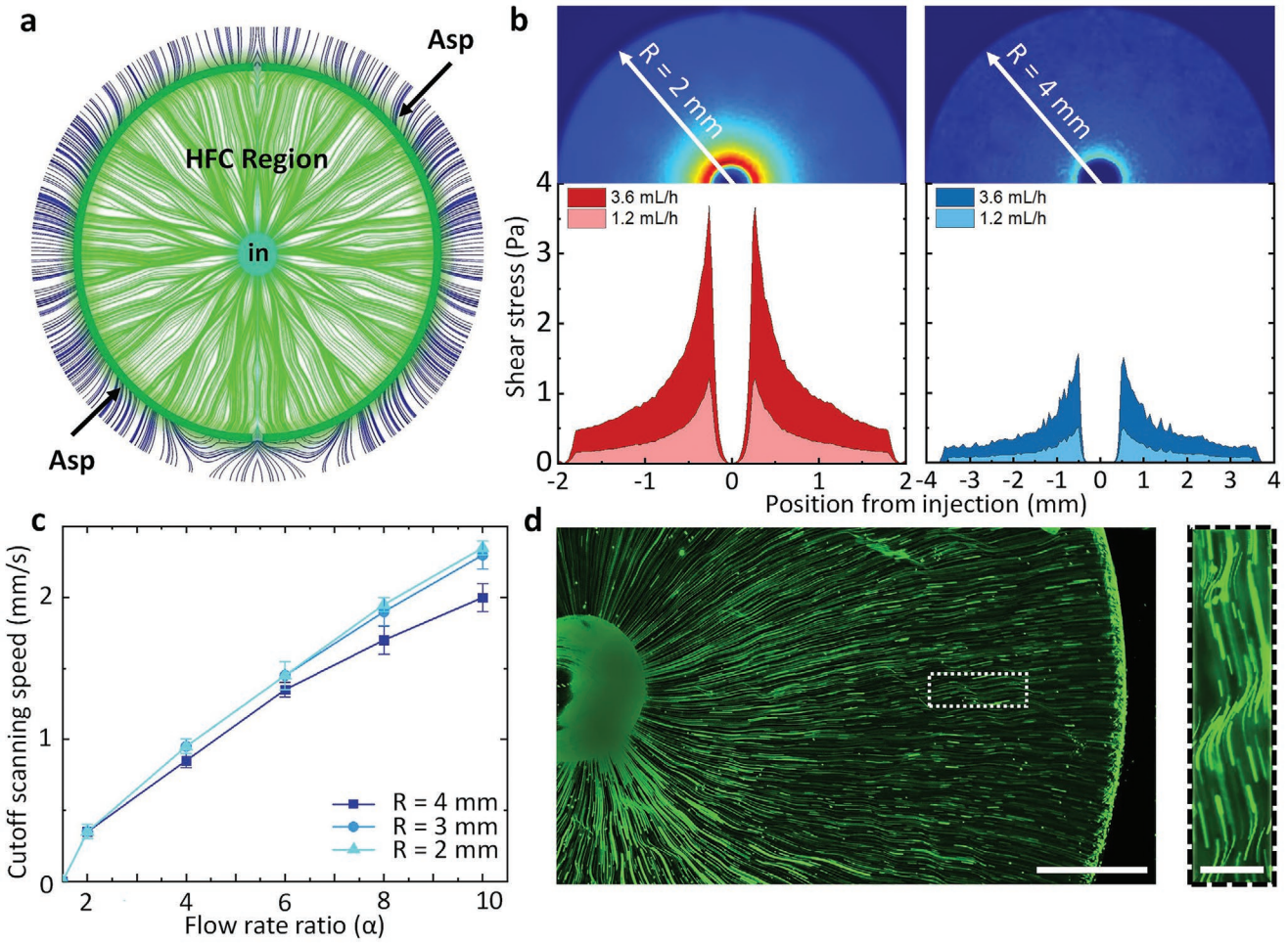

Figure 2. Parametric optimization of the HB-MFP. a) The plot of velocity streamlines (generated from a 3D finite element) shows the chaotic mixing induced by HB elements. The HFC region is indicated with green streamlines, where injection flow rate of 1.2 mL h^{-1} is used ($\alpha = 2$). The fluid is injected from the central aperture (in) and aspirated by the crescent-shaped apertures (Asp). b) Average shear stress with respect to spatial injection-to-aspiration distance under HB-MFP designs with $R = 2$ and 4 mm, and injection flow rates of 1.2 and 3.6 mL h^{-1}. With large fluid processing areas, the generated shear stresses are significantly reduced. c) The dependence of cutoff scanning speed on the ratio of flow rates (α) for various HB-MFP scales (R). A slight increase in cutoff scanning speed is observed with increased R. Values and error bars represent mean ± S.E.M ($n = 3$). d) Fluorescence image shows the helical motion of tracer microbeads (green) when introduced through the HB-MFP with $R = 4$ mm (Scale bar: 780 µm). Inset: An enlarged view of the boxed area (Scale bar: 60 µm).

cases, the separation distance "d" between the mesa and substrate was set to 50 µm, which represents a standard channel height in herringbone-based microfluidic chips.[20] Then, the shear stresses (τ) for both scales were numerically evaluated and compared. XY plots in Figure 2b clearly reveal an exponential decrease in shear stresses as fluid moves towards the aspiration apertures. Here, it is important to note that when the HB-MFP is designed with $R = 2$ mm, the shear stresses are 4 times higher than when designed with $R = 4$ mm. This is expected since τ has an inverse correlation with R and d. Furthermore, the average shear stresses in 80% of the 4 mm fluid processing area lie below 0.1 and 0.4 Pa for 1.2 and 3.6 mL h^{-1} injection flow rates, respectively (Figure 2b). Considering that blood has viscosity range of 3 to 4 mPa s,[39] this provides a suitable environment for the capture of viable CTCs. Thus, in line with the simulation results, in this work we adopted a processing area radius of 4 mm to minimize the shear stress and increase the HB-MFP throughput.

To study the effect of flow shear stresses on the capture efficiency, we next performed cell capture experiments by injecting a suspension of breast MCF-7 cells on anti-EpCAM antibody-activated glass slides at 0.6, 1.2, 2.4, 3.6, and 4.8 mL h^{-1} flow rates. Here, MCF-7 cells were used as model (positive control) for their known high expression of EpCAM.[40] Results in Figure S2 (Supporting Information) showed that when R is reduced from 4 mm to 3 and 2 mm, ≈20% and 50% drops in capture yield takes place, respectively, at flow rates <2.4 mL h^{-1}. Additional comparison with $R = 4$ mm revealed that the capture yield of $R = 3$ and 2 mm further drops by ≈95% at 2.4 mL h^{-1} flow rate, and by 100% (no capture) at 3.6 and 4.8 mL h^{-1} flow rates. These findings were attributed to the shorter travel paths of cells between the injection and aspiration apertures (i.e., less interaction with the capture antibodies) and the higher associated shear stresses.

An illustration of 2D flow maps for mesa regions with multiple combinations of simulated α, β, and φ is shown in Figure S3

(Supporting Information). When obtaining the maps, instances where HFC was either preserved or lost (i.e., when leakage took place in form of a hydrodynamic wake) were studied. As a result, cutoff scanning speeds (ω) were reconstructed for different α and R values and recorded (Figure 2c). Overall, the results revealed that higher values of ω can be reached with increased α and φ, where α has the most dominant effect. For instance, cutoff scanning speeds of as high as 2.35 mm s^{-1} were achieved with $\alpha = 10$ and $\varphi = 1.75$, and as low as 0.35 mm s^{-1} with $\alpha = 2$ and $\varphi = 1.25$. In order to put these values into perspective, the HB-MFP turns capable to fully scan a 75×25 mm^2 glass slide in 1 to 4 min, and with $\alpha > 10$, in less than a minute.

Another worthy of mention feature is the capability of the HB-MFP to operate with a wash-on-the-fly mode, see Figure S4a (Supporting Information). This mode is achieved by injecting the blood from one of the crescent-shaped apertures, while the washing fluid (e.g., PBS) is injected from the other. Both fluids are then aspirated from the central aperture. As for processing blood samples, where high throughput and low shear stresses are desired, maximum injection and minimum aspiration flow rates need to be applied (i.e., minimum α). This way, a cutoff scanning speed (e.g., 0.35 mm s^{-1}) would permit the full scan of a 75×25 mm^2 glass slide in about 15 min when 1 mL of blood is used. However, it is also noteworthy to mention that injecting blood from both crescent-shaped apertures while aspirating it from the central aperture (see Figure S4b-d, Supporting Information) will require higher aspiration-to-injection flow rate ratio to maintain the HFC, thus limiting the 2D scanning capabilities of the HB-MFP.

Next, we experimentally examined the microvortex generation effect of the incorporated radially designed HB elements, since the sole purpose of these elements is to achieve good capture efficiency of CTCs from blood. In this regard, a suspension of fluorescent beads (≈6 μm in diameter) was processed through the HB-MFP, and their path lines were recorded with time-lapse images. As shown in Figure 2d, with the influence of HB elements, the beads experienced a swirling effect and exhibited a helical 3D motion without compromising the HFC. Moreover, additional experiments with cells further demonstrated the significance of HB elements on the capture efficiency. In the experiments, the HB-MFP was redesigned and 3D printed to include HB elements only in half of the mesa, keeping the other half regularly flat as shown in Figure S5 (Supporting Information). As before, a suspension of MCF-7 cells was used as positive control and the bottom glass slide was functionalized with antibodies against EpCAM. With a 50 μm probe-to-substrate gap and using 1.2 mL h^{-1} injection flow rate, results revealed that the cell capture efficiency was increased by 56.8% in regions with HB elements compared to flat ones (i.e., without HB elements). This corresponds to ≈7 times enhancement in cell capture, clearly revealing the effectiveness of HB design in the HB-MFP. The HB design within closed microfluidic channels (e.g., HB-Chip), on the other hand, was reported to increase the capture efficiency by 26.3%.[20] Thus, the open-space design of HB-MFP additionally offers ≈2 times higher cell capture than the closed-space microfluidic channels.

2.3. Throughput and Cell Capture Efficiency

The following set of experiments were directed toward quantifying the throughput and cell capture efficiency of the HB-MFP, where various injection flow rates together with a range of probe-to-substrate gaps and cell concentrations were tested (**Figure 3**). After activating glass slides with anti-EpCAM antibodies, a suspension of the prostate (LNCaP and PC3), breast (MCF-7), and lymphoblastic (MOLT4) cells were injected through the HB-MFP. Here, MOLT4 cells were used as a negative control for nonspecific cell binding because of their known lack of EpCAM expression.[41] Additionally, a second negative control experiment was performed, where a suspension of lymphocyte (JKT) cells (also known for their lack of EpCAM expression[41]) was processed using the HB-MFP on an EpCAM-coated substrate. The non-specific capture of JKT was very low and matched well with the first negative control MOLT4 (Figure 3a).

Figure 3a shows the resulting cell capture yields with respect to the tested 1.2, 2.4, 3.6, and 4.8 mL h^{-1} injection flow rates, where the HB-MFP was positioned at 50 μm distance above the functionalized glass slide. For LNCaP, results revealed a maximum capture efficiency of 94.9% ± 1.4% at 1.2 mL h^{-1} flow rate, and a minimum capture efficiency of 38.8% ± 1.9% at 4.8 mL h^{-1} flow rate. Whereas for PC3 and MCF-7, the corresponding maximum (minimum) capture efficiencies were 79.7% ± 4.7% (24.8% ± 2.7%) and 95.6% ± 1.6% (41.1% ± 3.8%), respectively. Clearly, LNCaP and MCF-7 cells were captured at higher efficiencies compared to PC3 cells. This was attributed to higher expression of EpCAM in LNCaP and MCF-7,[42,43] although in our previous work we revealed, using flow cytometry, that EpCAM proteins are present in the surface of more than 75% PC3 cells.[22] Nevertheless, as expected, for all tested flow rates, the nonspecific binding of MOLT4 and JKT cells was below 8%. Fluorescence image in Figure 3b visualizes the distribution of PC3, MCF-7, and MOLT4 cells captured within one-third portion of anti-EpCAM-activated stripe at 1.2 mL h^{-1} flow rate, with least distributed ones corresponding to MOLT4 (negative control). Further investigation revealed that PC3 cells show a differential response to immunostaining of their nuclei (DNA), cytoplasmic cytokeratin (CK), and PSMA (Figure 3c).

The capture efficiency is strongly related with the magnitude of shear stresses, which is also greatly influenced by the separation distance "d" between the HB-MFP mesa and the capture substrate.[36] To investigate this effect on the cell capture efficiency, the HB-MFP was positioned at 25, 50, 75, and 100 μm distances above the substrate and a suspension of PC3 cells was injected on an anti-EpCAM-activated glass at 1.2 mL h^{-1} flow rate. As apparent in Figure 3d, with increasing separation distances, the cell capture efficiency increases until a maximum is reached, and then starts dropping down.

The low capture efficiency (≈43%) at 25 μm separation distance was attributed to the drastic increase in shear stresses as a result of the reduction in flow cross-sectional area. At distances beyond 50 μm, the shear stresses are gradually reduced. However, at these distances (i.e., 75 and 100 μm tested in this work), the interaction efficiency of cells with the capture antibodies is getting relatively reduced because of the enlarging gap that lowers the microvortex generation effect. On the other hand, the 50 μm separation distance provided an optimal cell

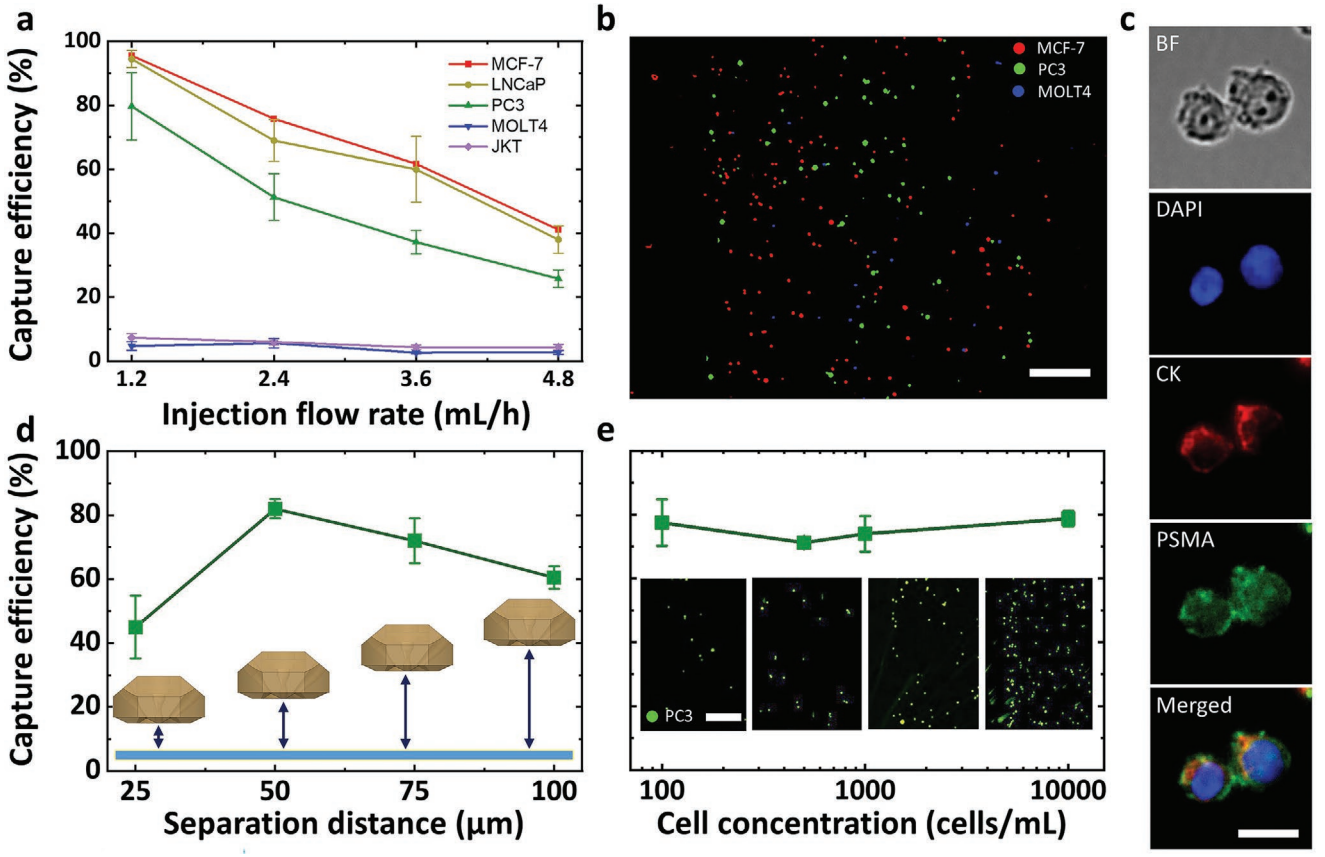

Figure 3. Throughput and cell capture efficiency investigation. a) Capture efficiencies of different cells types at flow rates ranging from 1.2 to 4.8 mL h^{-1} reveals the specificity of the capture against the surface expression of EpCAM molecules on MCF-7, LNCaP, and PC3 cells. MOLT4 and JKT cells are used as negative control. b) Fluorescence image shows the captured PC3 (green), MCF-7 (red), and MOLT4 (blue) cells on antibody stripe against EpCAM capture. For clarity, only one third portion of the stripe is shown. The non-specific binding of MOLT4 cells is minimal due to lack of EpCAM. Scale bar is 190 µm. c) Bright field and fluorescence images of captured PC3 cells reveal their shape, nucleus (blue, DAPI+), cytokeratin (red, CK+), and PSMA (green, PSMA+). Scale bar is 15 µm. d) Cell capture efficiency with respect to the separation distance "d" between the tip of the HB-MFP and the capture substrate (blue). e) Cell capture efficiency with different cell concentration suspensions. Inset: Example fluorescence images of captured PC3 cells (green) from samples with 100, 500, 1000, and 10 000 cells mL^{-1} concentrations. Scale bars is 420 µm. Values and error bars represent mean ± S.E.M ($n = 3$).

capture efficiency (≈82%) due to balancing of the two counter effects.

Further, we determined the device capture efficiency with a range of cell concentrations. Here, the HB-MFP was positioned at 50 µm above anti-EpCAM-activated glass slides and suspensions of PC3 (100, 500, 1000, and 10 000 cells mL^{-1} concentrations) were injected, separately, at 1.2 mL h^{-1} flow rate. As shown in Figure 3e, the capture efficiencies were consistent with all tested cell concentrations, indicating a capture efficiency between 70% and 80%. Given the consistent capture efficiency across different cell concentrations, we expect the same efficiency to be retained with lower cell concentrations (e.g., <100 cells mL^{-1}).

2.4. Multiplexed Capture of PC3 Cells

After device throughput and cell capture characterization, our next aim was to investigate the applicability of HB-MFP on multiplexed capture of PC3 cells when working in the scanning mode. To this end, each of the glass slides was activated with stripes of anti-EpCAM, anti-PSMA, and anti-PSA antibodies, and one stripe in between was left unmodified to serve as control experiment. Following, a suspension of PC3 and MCF-7 cells (mixed at equal concentrations) was injected through the HB-MFP using optimal working parameters. In this set of experiments, MCF-7 cells were used for investigating their non-specific binding on PSMA and PSA stripes. Cell capture was then carried out in scanning mode by exposing each stripe to equal volume of cell suspension (Figure 1b). Results showed that PC3 cells were captured on all three stripes (**Figure 4**a,b), with yields of ≈78% on EpCAM, 58% on PSMA, and 36% on PSA. The PC3 capture yield on the control stripe, on the other hand, was about 12%. As for MCF-7 cells, the capture yield was ≈90% on EpCAM stripe with negligible captures of <7% (comparable to control) on PSMA and PSA stripes. To sum, these outputs further demonstrated that the HB-MFP offers a versatile platform for multiplexed cell capture in 2D printing-like style, hovering atop different antibody stripes (Figure 4b), and capturing cells with high sensitivity and minimal nonspecific binding.

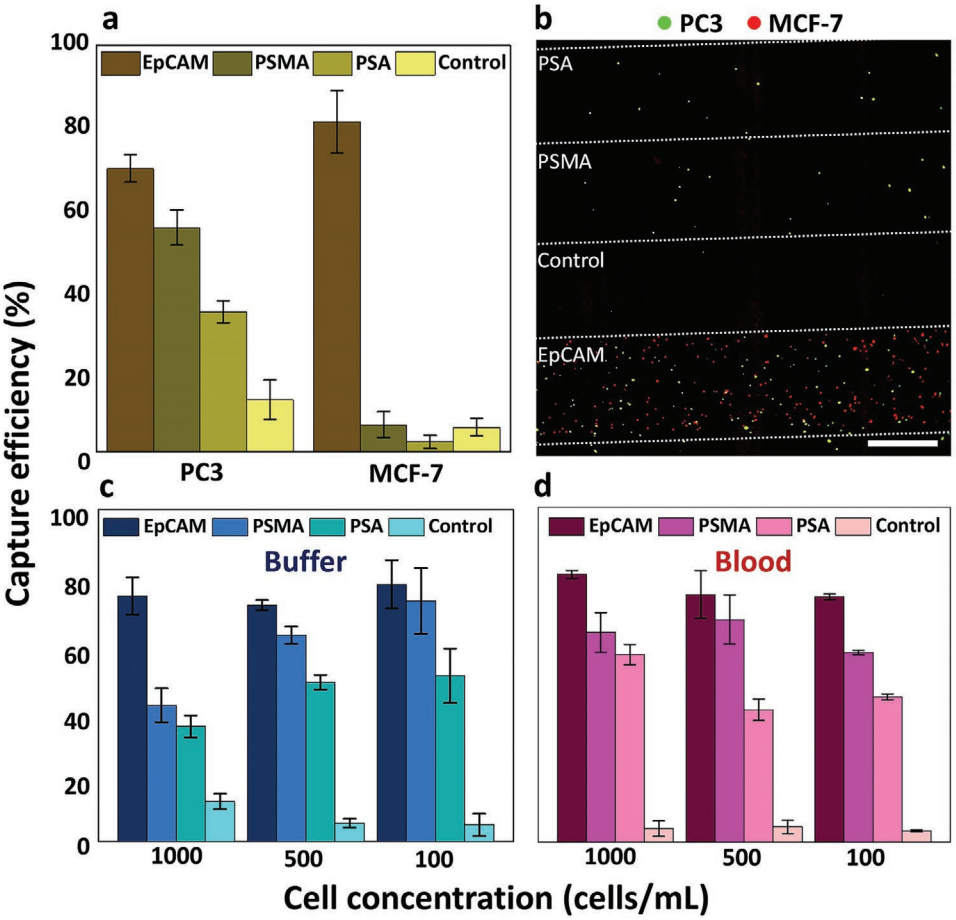

Figure 4. Multiplexed capture of PC3 cells. a) Capture efficiency of PC3 cells (spiked at equal concentration with MCF-7) on antibody stripes against EpCAM, PSMA, and PSA. In between, an unmodified stripe was left as a non-specific binding control. MCF-7 cells were used as control for their non-specific binding on PSMA and PSA stripes. b) Representative fluorescence image shows the distribution of captured PC3 (green) and MCF-7 (red) cells on the capture stripes. Increased capture of PC3 and MCF-7 cells was achieved on EpCAM stripes, whereas the capture of MCF-7 was minimal on PSMA and PSA stripes. Scale bar is 700 µm. c,d) Multiplexed capture of PC3 cells spiked in buffer and blood at various cell concentrations. Capture efficiency of ≈70–80% was observed on EpCAM stripes for all tested cell concentrations. Values and error bars represent mean ± S.E.M ($n = 3$).

Next, we directed our investigation of the multiplex capture when working with blood samples, where white blood cells (WBCs) and red blood cells (RBCs), along with cellular proteins and debris, could compete in the non-specific cell capture process. Therefore, additional experiments were carried using the HB-MFP, by processing PC3 cells, spiked in blood samples of healthy donors and in buffer (control), atop a substrate functionalized with EpCAM, PSMA, PSA, and control (no antibody) stripes. Results in Figure 4c,d portray the trends in cell capture efficiencies, where PC3 cell concentrations ranged from 100 to 1000 cells per mL spiked in buffer and blood. When spiked in blood, the capture purity of PC3 cells with reference to WBCs was ~11%, a result comparable to previously reported values.[20,22] Moreover, the similarity in capture yields of both sets suggests that the HB-MFP has the capacity to handle (with no clogging) viscous blood samples, and that the presence of WBCs, RBCs, and all other blood material has no significant effect on the multiplexed cell capture efficiency.

2.5. Multiplexed Capture of Prostate CTCs

Utilizing the optimized working conditions, we next moved toward clinical testing of the HB-MFP. For this, blood samples were collected from patients with localized and metastatic prostate cancer and processed through the HB-MFP using optimal parameters. The clinical information of patients comprised the following main parameters: PSA serum level, Gleason score (cancer grade), and age. In addition, patients' medical history and undergoing treatment type were also recorded (**Table 1**).

In CTC capture experiments, blood samples were processed in triplicates (with 1 mL used in each) by scanning the HB-MFP over a fresh substrate functionalized with antibody stripes against EpCAM, PSMA, and PSA. After thorough washing with buffer, cells that remained captured on the stripes were identified as CTCs (single or in form of clusters) based on the combined presence of their DNA, CK, and PSMA, revealed by fluorescent staining (**Figure 5**a,b). WBCs, on the other hand, were positive for their transmembrane

Table 1. Clinical information of patients and number of captured CTCs using the HB-MFP.

Patient ID	PSA Serum [ng mL^{-1}]	Gleason Score (Cancer Grade)	Age	Medical history/undergoing treatment	Cancer identification	Captured CTCs per mL
1	0.072	7 (3 + 4) (Grade 2)	64	Tumor removed/radiation therapy (recovering patient)	Localized	6
2	8	7 (3 + 4) (Grade 2)	46	Castration sensitive/radiation therapy	Localized	9
3	24	7 (3 + 4) (Grade 2)	68	Treatment naïve	Localized	17
4	48	9 (4 + 5) (Grade 5)	62	Castration resistant	Metastatic	32
5	47	7 (4 + 3) (Grade 3)	76	Castration sensitive/radiation therapy	Metastatic	32
6	15	9 (4 + 5) (Grade 5)	47	Castration resistant/hormone therapy	Metastatic	34
7	48	9 (4 + 5) (Grade 5)	54	Treatment naïve	Metastatic	187
8	6	9 (4 + 5) (Grade 5)	63	Castration resistant/Hormone therapy (no response to treatment)	Metastatic	280
9	1	7 (4 + 3) (Grade 3)	52	Hormone therapy	Metastatic	24

CD45 staining and negative for PSMA staining (Figure S6, Supporting Information).

Overall results revealed the presence of CTCs in all patients (Table 1), with counts ranging from 6 to 280 CTCs mL^{-1}. Among them, number of CTCs captured from patients with localized cancer (P1, P2, & P3) were between 5 to 17 CTCs mL^{-1} (10.5 ± 3.3, mean ± SD), with 5 ± 2, 3 ± 1, 2 ± 1 CTCs mL^{-1} distribution on EpCAM, PSMA, and PSA stripes, respectively (Figure 5c). The number of CTCs captured from patients with metastatic cancer (P4, P5, P6, P7, P8 & P9), on the other hand, were between 32 and 280 CTCs mL^{-1} (98.2 ± 44.5, mean ± SD), with 47 ± 18, 35 ± 18, 13 ± 6 CTCs mL^{-1} distribution on EpCAM, PSMA, and PSA stripes, respectively (Figure 5c).

It is known that EpCAM and PSMA are most common transmembrane proteins expressed by prostate CTCs and that the level of expression of these proteins varies with the tumor progression and indicates certain cellular behaviors.[30] For example, the overexpression of EpCAM is correlated with increased cell proliferation,[44] and that of PSMA with higher cancer grade (invasiveness) and androgen deprivation.[45,46] Whereas the downregulation of EpCAM expression occurs during epithelial-to-mesenchymal transition (EMT),[44] and that of PSMA during androgen receptor reactivation.[46] PSA, on the other hand, is secreted by CTCs[47] and its expression is upregulated during androgen receptor reactivation and downregulated during the androgen deprivation.[46] In contrast to EpCAM, which is shown to be also expressed on hematopoietic lineage cells,[19] PSMA and PSA are highly specific to prostate cancer and PSMA expression, in particular, is known not to be altered by EMT-induced cellular changes.[48]

In typical closed-channel microfluidic devices, CTCs are captured only through positive selection of EpCAM,[49] which brings unknown biases especially when cells are undergoing EMT.[49–51] As a result, increasing evidences suggest that the EpCAM-based CTC capture and enumeration is associated with poor prognosis.[48,51] Notably, in our study, results in multiplex profiles revealed the particular importance of PSMA and PSA as capture molecules to assist or even substitute EpCAM, where CTCs captured on each of the different antibody stipes revealed distinct counts for each patient (Figure 5c). Because of specific antibody-antigen association, the distinct counts could be correlated with PSMA and PSA expression levels to provide unbiased information about the invasiveness and treatment response of CTCs. For example, for patient P7 the average number of CTCs captured on PSMA and PSA stripes were 64 ± 23 and 41 ± 19, respectively. While for patient P8, the corresponding CTC numbers read 112 ± 20 and 21 ± 11. At the time of blood collection, both patients were diagnosed with grade 5 cancer, where P7 was treatment naïve and P8 was castration resistant with undergoing hormonal (androgen deprivation) therapy (Table 1). When compared, the 43% increment in number of CTCs captured on PSMA stripes and the 49% capture drop on PSA stripes revealed correlation with the undergoing therapy on patient P8. This finding is evident with the fact that when treatment naïve patients undergo androgen deprivation therapy, PSMA expression on CTCs is increased while PSA expression is reduced.[46]

Moreover, within the grade 5 castrate-resistant patients (P4, P6, & P8), the number of captured CTCs on PSA stripes correlated well with the PSA serum levels of the patients (Table 1), where 69% drop in PSA serum level reflected 41% increment in PSA capture. When the drop in PSA serum level was about 88%, the increment in PSA capture was 81%. Combined, PSA-captured CTCs correlated well with PSA serum levels in comparison to EpCAM and PSMA captures (Figure 5d–f). This finding, which is attributed to the treatment-induced PSA secretion in castrate-resistant CTCs,[52] further asserts that PSA serum levels need to be evaluated along with PSA expression

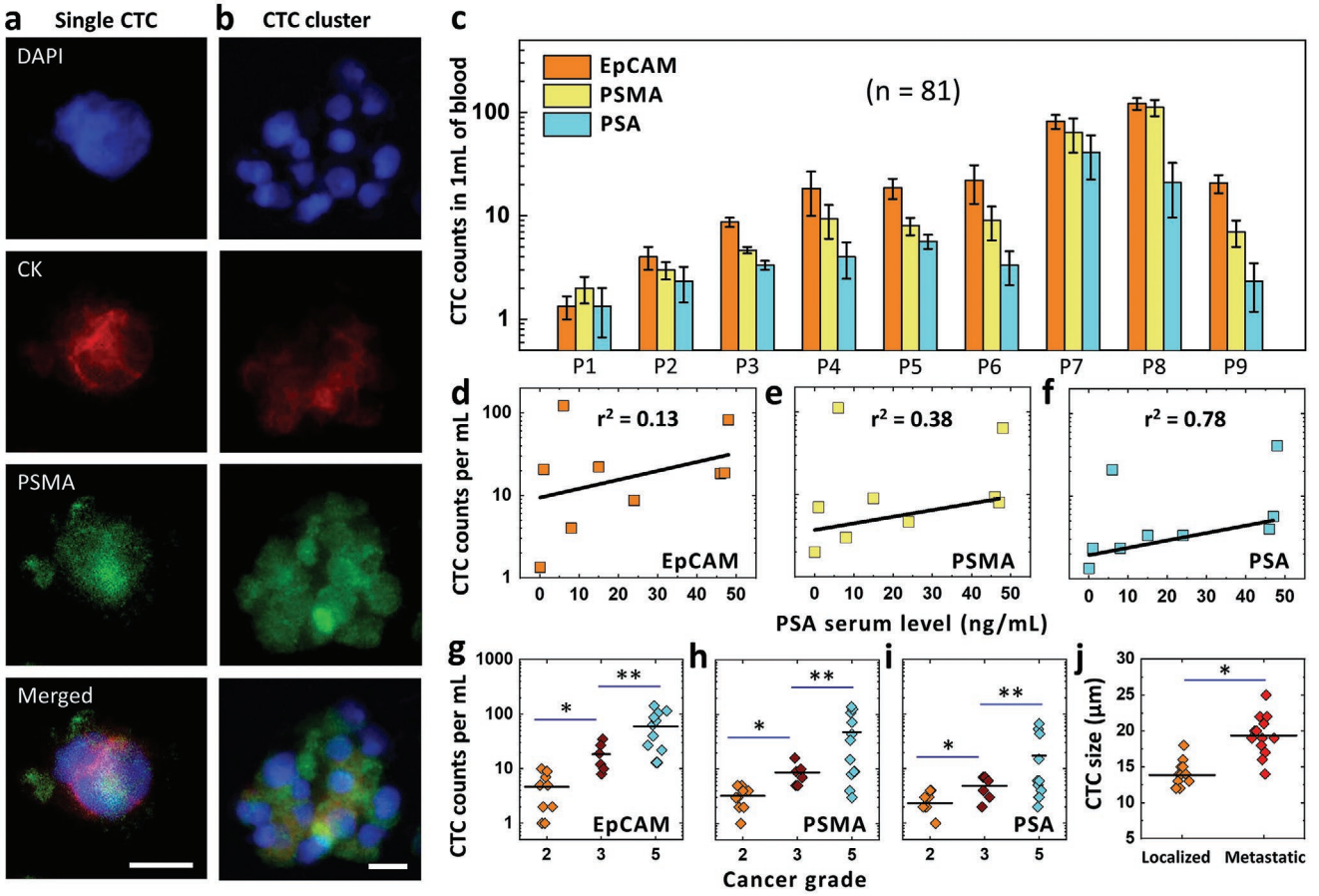

Figure 5. Multiplexed capture and profiling of prostate CTCs. a,b) Representative fluorescence images of captured single and cluster CTCs are shown positive to immunostaining of their nucleus (blue, DAPI+), cytokeratin (red, CK+), and PSMA (green, PSMA+). Scale bars are 15 µm. c) Logarithmic plot of single CTCs captured on EpCAM, PSMA, and PSA stripes from 1 mL peripheral blood of patients with localized (P1, P2 & P3) and metastatic (P4, P5, P6, P7, P8, & P9) backgrounds. The presence of CTCs was revealed in all patients. Values and error bars represent mean ± S.E.M. d–f) The correlation between patients' PSA level and the number of captured CTCs on EpCAM, PSMA, and PSA stripes suggests that PSA expression levels need to be considered along with PSA serum levels for the response to applied therapy. g–i) Association between clinical cancer grade and CTCs captured on the EpCAM, PSMA, and PSA stripes reveals that cancer grade 5 patients has highest mean expression level of antigens, followed by antigens in cancer grades 3 and 2 patients. j) The size distribution for CTCs captured from localized and metastatic prostate cancer patients is consistent with reported values. *&** denote statistically significant at $P < 0.05$ using t-test.

levels during the cancer progression.[53] As such, decrease in PSA serum levels may reflect positive response (i.e., androgen receptor deactivation) in castrate-resistant patients to applied therapy. However, the increase in PSA expression in CTCs suggests that androgen signaling may not be fully deactivated.[46] Although, this finding could support the intrapatient and interpatient heterogeneity in androgen receptor activity of CTCs,[46] further investigation involving more patients is left for future studies.

The multiplex profiles could also provide clues to metastatic activity of CTCs and help in differentiating the cancer grades between patients (Table 1). For example, the multiplex profile of patient P1 revealed that the CTC capture on EpCAM stripe is 50% less than on PSMA stripe, which could be associated with the reduced EpCAM expression on cells undergoing EMT,[44] see Figure 5c. Additionally, the number of CTCs captured on EpCAM, PSMA, and PSA stripes revealed significantly distinct average counts to help in differentiating the cancer grades 2, 3, and 5 (Figure 5g–i). As stated before, due to specific antibody–antigen association, these counts could be correlated with the respective antigen expression levels. With this assumption, overall results suggested that antigens in cancer grade 5 patients show highest mean expression level, followed by antigens in cancer grades 3 and 2 patients.

Interestingly, however, the distributions of EpCAM, PSMA, and PSA expression levels in cancer grade 5 patients were relatively more dispersed, with upper values belonging to P7 and P9 patients and lower values to P4 and P6 patients (Figure 5g–i). This finding could potentially indicate a better response to therapy in patients P4 and P6. The distributions of PSMA and PSA expression levels in cancer grade 2 patients (localized cancer), on the other hand, were more localized compared to EpCAM (Figure 5g–i), thereby suggesting that PSMA and PSA could represent better alternative in differentiating low-grade tumors. Clearly, the clinical aspects of our findings are all intriguing. However, for statistical significance, a higher number of patients need to be taken into account in the future studies.

Nevertheless, while most of the captured CTCs were single cells (Figure 5a), cell clusters comprising 8 to 10 CTCs were also captured from blood samples of 3 out of 5 patients with metastatic background (Figure 5b). Remarkably, in one case, the size of the captured cluster reached 40 to 50 CTCs (Figure S7, Supporting Information). The cluster formations are known to represent a form of survival for CTCs in the harsh microenvironment of blood circulatory, and are highly associated with tumor metastatic potential and negative response to treatments.[54] Obviously, the isolation of these large clusters would be extremely difficult to achieve in closed microfluidic devices, as clusters would either tend to disintegrate due to high flow resistance within the narrow channels or clog the channels before reaching the capture substrate. On a final note, the average size of single CTCs was 13.8 ± 1.8 μm in patients with localized cancer and 19.4 ± 2.8 μm in patients with metastatic cancer (Figure 5j). These values are within the range of previously reported sizes.[22,55,56]

3. Discussion

The HB-MFP is developed for multiplexed capture of CTCs on an open substrate. Its design allows to work with any independent flat surface, permits capture in 2D printing style, provides enhanced throughput and cell capture efficiency, and favors cell integrity and viability. The design of HB-MFP is modular and can be re-adjusted in size and position to fit any working condition. In this work, the HB-MFP included a central aperture for injection, two outer crescent-shaped apertures for aspiration, and radially staggered herringbone elements for high throughput blood processing with minimal associated shear stresses. As a result, the shear stress gradient generated within 80% of its processing area lied below 0.4 Pa for flow rates up to 3.6 mL h^{-1}, thus favoring the efficient capture of intact and viable single CTCs as well as their intact clusters. The remaining 20% of the injection zone resulted in relatively higher shear stress; yet with no significant impact on the capture efficiency.

Moreover, with the HB-MFP, the blood delivery system is independent of the capture substrate, thus allowing for postanalysis of captured CTCs without the need of their release. In standard closed-channel microfluidic devices, the release of CTCs is usually followed by applying additional chemical processes or shear stresses, both of which could damage their fragile nature and limit the downstream analysis.[57] The obstacle is that the channels, residing in polydimethylsiloxane (PDMS) layer, are assembled to the glass substrate via permanent covalent bonding, therefore preventing the external reach to the cells. Our previous efforts to apply reversible microfluidic chip proved successful in characterizing captured prostate CTCs using atomic force microscopy (AFM).[22] However, in the work, the transition from cell capture and identification to cell characterization was still susceptible to cell loss, which was associated with peeling off the PDMS. The HB-MFP, on the contrary, is gently (in a controlled manner) pulled away from the capture substrate, permitting access of captured cells in a seamless way without loss or dislocation. Downstream analysis on captured CTCs could then be performed for drug delivery, secretome, and transcriptome response, and nanomechanical characterization using AFM.

The HB-MFP is cheaply 3D printed: it can be reproduced in an hour and its design can be easily modified to suit any specific experiment. For example, by varying the design of its apertures and their separation distances, the device could provide flexibility in adjusting the size and shape of the HFC footprint, and as well, bigger processing areas could be obtained without compromising the flow resistance. Processing areas can be easily utilized for scaling up throughput and multiplexed capture, where large blood volumes can be processed with significantly higher flow rates but without exposing the blood content to high shear stresses and evading saturation. In addition, the HB-MFP can be autoclaved and reused multiple times. Furthermore, because of its scanning capability, the capacity of the HB-MFP to thoroughly wash-on-the-fly the substrate comes as important benefit. In case of closed microfluidic chips, the risk for the PDMS walls to collapse limits the channel width, thus resulting in limited space to process fluids. Also, attempts to section large channel widths into narrow ones come at the expense of higher flow resistance, and hence, higher shear stresses.

With its open-space design, the HB-MFP also offers a versatile tool for multiplexed capture of prostate CTCs through their specific EpCAM, PSMA, and PSA antigens. Here, the multiplexing is attributed when the whole blood sample is simultaneously processed for the three capture profiles. However, the multiplexing can be further designed to include tens of other recognition molecules within any desired patterns. In our previous work, we showed that EpCAM, PSMA, and PSA antigens could be all effective for specific capture of CTCs.[22] Although successful, simultaneous processing of blood samples in three separate microfluidic chips limited the throughput for post-capture identification of CTCs. The open-space design of the HB-MFP, on the other hand, paved the way to quickly hover blood samples over the activated antibody stripes and gave access to captured CTCs for their fluorescence staining without noticeable cell loss. As a result, in this work, the specificity of multiplexing was utilized for the rapid separation of CTCs based on their EpCAM, PSMA, and PSA expressions because only CTCs with the targeted antigens would be captured on the stripes modified with corresponding antibody.

The resulting multiplex profiles not only enhanced the overall cell capture efficiency, but also aided in phenotyping CTCs for targeted therapy. As such, capturing CTCs through their PSMA and PSA provided information on invasiveness, treatment response, and metastatic activity of CTCs, and helped in differentiating the cancer grades between patients. This finding was particularly important, since commonly used EpCAM-based CTC capture methods could be biased due to loss of protein expression during the EMT. Moreover, it is acknowledged that PSMA and PSA contribute significantly to mutations within the prostate CTCs associated with androgen receptor signaling;[46] and hence, constitute biomarkers for the assessment of treatment effectiveness and overall patient survival. Thus, and considering the clinical importance as biomarkers and therapeutically relevant targets,[49,58] PSMA- and PSA-based capture hold a great promise to phenotype CTCs. However, with the existing microfluidics approaches, their molecular characterization (and our understanding of their relationship with androgen receptor signaling status)

commonly rely on multi-fluorescence staining of captured CTCs and subsequent use of complex image processing and analysis. With the present work, on the other hand, the CTC separation and phenotyping is solely based on multiplex antibody-antigen association. With these aspects, the HB-MFP can help in acquiring a wealth of information on CTCs on a patient basis. Consequently, not only the number of CTCs captured on each distinctive antibody could be correlated with patients' clinical profiles, but also their molecular characteristics could be explored for each patient in an efficient way.

Another important aspect of using HB-MFP is that the cancer material can be captured as it is present in the blood. For example, with the HB-MFP capturing CTC clusters comprising as many as 50 cells is achievable. Such clusters are of a high research importance due to their association with metastasis in many reports,[59] and are difficult to capture using the common closed-channel microfluidic devices.[26] Importantly, the HB-MFP can also be applied to other types of cancer such as breast cancer by simple adjustments, where multiplex capture could include human epidermal growth factor receptor 2 (HER2) as a recognition molecule along with EpCAM. Given the open nature of the system, the bottom glass substrate can also be functionalized with any type of recognition receptors such as antibodies, aptamers, nanowires, RNAs, or graphene oxide nanosheets.[60–62]

In conclusion, in this work the open-space microfluidics combined with the micro vortex generating herringbone was explored in the field of liquid biopsy. In the course, the HB-MFP was designed, parametrically characterized, 3D printed, and optimized to achieve highest throughput and cell capture efficiency. Moreover, the scanning capacity of the HB-MFP demonstrated a versatile tool for multiplexed capture of CTCs (single or in form of clusters) from prostate cancer patients with localized and metastatic backgrounds. The HB-MFP could serve as a feedback system on the efficacy of implemented treatment strategies, as a mean for drug testing, or simply, as an early diagnostic tool.

4. Experimental Section

Chemicals, Reagents, and Materials: Phosphate buffered silane (PBS), Roswell Park Memorial Institute (RPMI) medium, and Dulbecco's modified Eagle medium (DMEM) were purchased from Invitrogen. Bovine serum albumin (BSA), trypan blue exclusion assay, TrypLE express enzyme, CellTracker fluorescent dyes (green, red, and blue), green fluorescent beads (≈6 µm in diameter), 3-mercaptopropyl trimethoxysilane (MPTMS), N-y-mal-eimridobutyryloxy succinimide ester (GMBS), and NeutrAvidin were purchased from ThermoFisher Scientific. Fetal bovine serum (FBS) and penicillin-streptomycin (Pen-Strep) solution were purchased from Sigma-Aldrich. Biotinylated anti-human monoclonal 9C4, YPSMA-1, and C-19 antibodies against EpCAM, PSA, and PSMA antigens, respectively, together with anti-human monoclonal PSMA antibodies conjugated to Alexa 488 (green) were purchased from Santa Cruz Biotechnology. Human prostate cancer cells (LNCaP and PC3), breast cancer cells (MCF-7), lymphoblastic T cells (MOLT4), and lymphocyte Jurkat T cells (JKT) were purchased from American Type Culture Collection.

Numerical Modeling: 3D finite element (COMSOL Multiphysics) was used to produce the 3D numerical models of the HB-MFP. Numerical solutions were obtained using direct and stationary solver to compute the Navier-Stokes equation (laminar and no-slip wall conditions) coupled with the transport of diluted species (convection-diffusion) equations. The HB-MFP was modeled as a circular surface with inlet and outlets that corresponded to the injection and aspiration apertures. Its simulation dimensions were similar to the 3D printed HB-MFP. Parametric characterization was carried out as a function of ratio of aspiration/injection flow rates (α), scanning speeds (β), and mesa/processing areas (φ). A 3D model was built and a mesh sensitivity test was performed to ensure sufficient element density. For each simulation, the injection flow rate, the diameter of the footprint, and the gap between the mesa and the substrate were kept at constant values. On the other hand, aspiration flow rate and mesa area values were varied with different scanning speeds.

HB-MFP Fabrication and Platform Assembly: The HB-MFP was designed using CAD software (SolidWorks), and manufactured using Solus DLP stereolithography 3D printer using SolusProto resin (Junction3D). Afterwards, the 3D printed HB-MFP was thoroughly washed with ethanol, UV cured for 2 min, and again washed with deionized (DI) water. Then, a twist-lock arm was produced using Dimensions SST 1200es 3D printer (Stratasys) to connect the HB-MFP to XYZ linear motorized stage with built-in controller (X-LRM, Zaber Technologies). Following, the setup was integrated with the stage of ECLIPSE Ti inverted epifluorescence microscope (Nikon), which was equipped with DS-Qi2 monochrome camera and DAPI, FITC, and Texas Red filter cubes. Finally, neMESYS high precision syringe pump (Cetoni GmbH) was used to inject and aspirate the fluid through the HB-MFP.

Glass Substrate Cleaning and Activation: 75 mm × 25 mm glass microscope slides (J. Melvin Freed) were ultrasonically cleaned in DI water and ethanol for 3 min and dried with nitrogen. In the meantime, four microfluidic channels (implemented with CAD design for glass antibody activation) were 3D printed and PDMS molded. Then, the channels (each 1 mm wide, 100 µm deep, and 21 mm long) were placed onto glass slides and transferred to a 60 °C oven for 2 h for a reversible bonding. Afterwards, the activation of glass slides was accomplished using avidin–biotin chemistry.[63] In brief, a solution of ethanol containing 1 wt% MPTMS was passed through the channels and incubated for 45 min. After silanization, ethanol was passed through channels to remove loosely bound silane molecules. Then, 1 wt% solution of GMBS in ethanol was injected into the channels and incubated for 30 minutes. Following, channels were washed with ethanol, DI water, and PBS. GMBS-activated glass slides were then incubated in 1 wt% NeutrAvidin solution in PBS for 1 h. PBS was then passed to remove loosely bound NeutrAvidin molecules. Finally, biotinylated anti-EpCAM, anti-PSMA, and anti-PSA antibodies (10 µg mL^{-1} concentration in PBS) were passed through three of the channels and incubated for 1 h. The remaining one channel was left unmodified (control). PBS was again passed to remove unbound antibody molecules. This was followed by introducing 1% (v/v) BSA solution for 20 min to block nonspecific binding sites on the glass. The PDMS layers were then peeled off and antibody-activated glass slides were immersed in PBS in Petri dishes for further device throughput and cell capture optimization experiments.

Cell Culture: LNCaP and PC3 cells were used as model prostate cancer cell lines in device throughput and cell capture optimization experiments. Whereas MCF-7 cells were used as a positive control for their high expression of EpCAM, and MOLT4 and JKT cells were used as a negative control for their nonspecific binding. Prior to each experiment, PC3 cells and T cells were grown in an RPMI medium, and MCF-7 cells in a DMEM medium. In both cases, the culture media was supplemented with 10% FBS and 1% Pen-Strep, and cells were placed in a 37 °C humidifying incubator supplemented with 5% CO_2. After three to four passages, cells (about ≈80% confluent) were washed three times with PBS and labeled using CellTracker fluorescent dyes. Following, cells were trypsinized using TrypLE and centrifuged at 900 rpm for 5 min. The cell pellets (≈10^6 cells) were then resuspended in fresh culture medium. Trypan blue exclusion assay was applied to directly count the number of live cells using Countess II FL (FisherScientific) automated cell counter. Later, cells at various concentrations were spiked into 1 mL of either culture medium or healthy donor blood samples.

Throughput and Cell Capture Optimization: Throughput optimization was carried by injecting fluorescently-labeled LNCaP, PC3, MCF-7, and MOLT4 cells (spiked into 3 mL of culture medium at 5000 cells mL^{-1} concentrations) at 1.2, 2.4, 3.6, and 4.8 mL h^{-1} flow rates onto anti-EpCAM antibody-activated glass slides, where the flow rates were controlled with the neMESYS syringe pump. The cell suspensions were loaded into a neMIX stirring bottle (Cetoni GmbH) to avoid cell sedimentation. Separately, the experiment was repeated only with JKT cells for their non-specific binding. In addition, prior to all experiments, BSA was passed through the tubes and the HB-MFP for 20 min to prevent additional cell settling (through sedimentation).

Cell capture optimization was carried by spiking PC3 and MCF-7 cells in 1 mL culture medium at concentrations of 100, 500, 1000, and 10 000 cells mL^{-1} and injecting onto anti-EpCAM antibody-activated glass slides at a 1.2 mL h^{-1} flow rate. Following, the capture efficiencies of cells were recorded in a logarithmic scale as a function of spiked number of cells. In addition, the effect of HB-MFP separation distance was investigated by injecting PC3 cells (spiked in 1 mL culture medium at 1000 cells mL^{-1} concentration) onto anti-EpCAM antibody-activated stripes at a 1.2 mL h^{-1} flow rate.

Multiplexed cell capture was carried by injecting a mixture of PC3 and MCF-7 cells (spiked into 2 mL of medium at concentrations 500 cells mL^{-1} for each) at 1.2 mL h^{-1} flow rate onto antibody stripes against EpCAM, PSMA, and PSA, and a control (no antibody) stripe in between. Then, in same way, PC3 cells (spiked in 1 mL culture medium per healthy donor blood samples at 100, 500, 1000, and 10 000 cells mL^{-1} concentrations) were processed on multi-activated glass substrates.

In all optimization experiments, detection and counting of captured cells were carried with a 10× air objective lens and using DAPI, FITC, and Texas Red filter cubes. The capture efficiency was then calculated as follows: The cells were first counted manually at the outlet of the device while exiting the processing area, and then within the processing area when captured. The number of captured cells was then divided to the sum of all counted cells and recorded as percentage of cell capture (i.e., $\frac{\text{Captured cells}}{\text{Captured cells} + \text{Aspirated cells}} \times 100$). In case of multiplexed capture experiments, the capture efficiencies were calculated in same way, but independently for each stripe.

Blood Collection and CTC Capture and Identification: Blood samples were collected from 3 healthy donors and from 9 patients with localized and advanced prostate cancer at Mediclinic City Hospital in Dubai, UAE. In agreement with NYU Abu Dhabi Institutional Review Board (IRB)-approved process, the blood samples were transferred in tubes containing ethylenediaminetetraacetic acid (EDTA) and processed through HB-MFP within 8 hours of blood draw. Healthy blood samples were used for device optimization experiments using spiked PC3 cells, whereas patient blood samples were used for capture of CTCs.

As with the cell lines, the multiplexed capture of CTCs was accomplished using stripes of antibodies against EpCAM, PSMA, and PSA. After thorough washing stripes with PBS, the captured CTCs were stained with anti-human monoclonal $PSMA^+$ antibodies conjugated to Alexa 488 (excitation maximum 490 nm and emission maximum 525 nm) for 20 min. Afterwards, they were immunostained for DAPI (nucleus) and cytoplasmic cytokeratin, and identified and counted using 40× air objective lens. Open-source software ImageJ was used to process fluorescent images.

Statistical Analysis: Statistical analysis was performed with Origin software using two-sample t-test analysis to evaluate size differences of CTCs of localized and metastatic backgrounds. A P-value of <0.05 was considered statistically significant. Values and error bars represent mean ± S.E.M. of at least triplicate experiments.

Supporting Information

Supporting Information is available from the Wiley Online Library or from the author.

Acknowledgements

M.D. and P.S. contributed equally to this work. This study was financially supported by NYU Abu Dhabi, the 2017 NYU Abu Dhabi Research Enhancement Fund, UAE, and the Terry Fox Foundation's International Run Program, Vancouver, Canada. The authors acknowledge the NYU Abu Dhabi Grants for Publication Program. The authors greatly acknowledge the patients, donors, and nurses for blood donation and collection, and the Core Technology Platforms at NYU Abu Dhabi for the technical support. A.G. and A.T.B. acknowledge the NYUAD Global PhD Fellowship.

Conflict of Interest

The authors declare no conflict of interest.

Data Availability Statement

The data that support the findings of this study are available from the corresponding author upon reasonable request.

Keywords

antigen–antibody capture, circulating tumor cells, herringbone chaotic mixing, liquid biopsy, microfluidics, scanning probes

Received: January 17, 2021
Revised: March 13, 2021
Published online:

[1] R. L. Siegel, K. D. Miller, A. Jemal, *Ca-Cancer J. Clin.* **2020**, *70*, 7.
[2] C. L. Chaffer, R. A. Weinberg, *Science* **2011**, *331*, 1559.
[3] F. Macedo, K. Ladeira, F. Pinho, N. Saraiva, N. Bonito, L. Pinto, F. Goncalves, *Oncol. Rev.* **2017**, *11*, 43.
[4] R. Etzioni, N. Urban, S. Ramsey, M. McIntosh, S. Schwartz, B. Reid, J. Radich, G. Anderson, L. Hartwell, *Nat. Rev. Cancer* **2003**, *3*, 243.
[5] J. H. Liu, Y. R. Liu, D. L. Yang, C. H. Yang, L. J. Mao, *Discovery Med.* **2019**, *27*, 235.
[6] T. H. Phillips, I. M. Thompson, *Urol. Clin. North Am.* **1991**, *18*, 459.
[7] H. G. T. Nijs, M. L. Essink-Bot, H. J. DeKoning, W. J. Kirkels, F. H. Schroder, *J. Public Health Med.* **2000**, *22*, 312.
[8] D. S. Smith, A. D. Bullock, W. J. Catalona, *J. Urol.* **1997**, *158*, 1861.
[9] W. J. Catalona, J. P. Richie, F. R. Ahmann, M. A. Hudson, P. T. Scardino, R. C. Flanigan, J. B. DeKernion, T. L. Ratliff, L. R. Kavoussi, B. L. Dalkin, W. B. Waters, M. T. MacFarlane, P. C. Southwick, *J. Urol.* **2017**, *197*, 200.
[10] I. M. Thompson, *New Engl. J. Med.* **2004**, *351*, 2021.
[11] G. Botchorishvili, M. P. Matikainen, H. Lilja, *Curr. Opin. Urol.* **2009**, *19*, 221.
[12] Y. Wan, M. Winter, B. Delalat, J. E. Hardingham, P. K. Grover, J. Wrin, N. H. Voelcker, T. J. Price, B. Thierry, *ACS Appl. Mater. Interfaces* **2014**, *6*, 20828.
[13] M. Ilie, V. Hofman, E. Long, O. Bordone, E. Selva, K. Washetine, C. H. Marquette, P. Hofman, *Ann. Transl. Med.* **2014**, *2*, 107.
[14] C. A. Klein, *Nat. Rev. Cancer* **2009**, *9*, 302.
[15] I. Desitter, B. S. Guerrouahen, N. Benali-Furet, J. Wechsler, P. A. Janne, Y. A. Kuang, M. Yanagita, L. L. Wang, J. A. Berkowitz, R. J. Distel, Y. E. Cayre, *Anticancer Res.* **2011**, *31*, 427.
[16] J. P. Shelby, J. White, K. Ganesan, P. K. Rathod, D. T. Chiu, *Proc. Natl. Acad. Sci. USA* **2003**, *100*, 14618.

[17] L. M. Broche, N. Bhadal, M. P. Lewis, S. Porter, M. P. Hughes, F. H. Labeed, *Oral Oncol.* **2007**, *43*, 199.
[18] S. Balasubramanian, L. H. Hurley, S. Neidle, *Nat. Rev. Drug Discovery* **2011**, *10*, 261.
[19] E. E. van der Toom, H. D. Axelrod, J. J. de la Rosette, T. M. de Reijke, K. J. Pienta, K. C. Valkenburg, *Nat. Rev. Urol.* **2019**, *16*, 7.
[20] S. L. Stott, C. H. Hsu, D. I. Tsukrov, M. Yu, D. T. Miyamoto, B. A. Waltman, S. M. Rothenberg, A. M. Shah, M. E. Smas, G. K. Korir, F. P. Floyd, A. J. Gilman, J. B. Lord, D. Winokur, S. Springer, D. Irimia, S. Nagrath, L. V. Sequist, R. J. Lee, K. J. Isselbacher, S. Maheswaran, D. A. Haber, M. Toner, *Proc. Natl. Acad. Sci. USA* **2010**, *107*, 18392.
[21] M. A. Qasaimeh, Y. C. Wu, S. Bose, A. Menachery, S. Talluri, G. Gonzalez, M. Fulciniti, J. M. Karp, R. H. Prabhala, R. Karnik, *Sci. Rep.* **2017**, *7*, 45681.
[22] M. Deliorman, F. K. Janahi, P. Sukumar, A. Glia, R. Alnemari, S. Fadl, W. Q. Chen, M. A. Qasaimeh, *Microsyst. Nanoeng.* **2020**, *6*, 20.
[23] S. Regmi, A. Fu, K. Q. Luo, *Sci. Rep.* **2017**, *7*, 39975.
[24] S. D. Mikolajczyk, L. S. Millar, P. Tsinberg, S. M. Coutts, M. Zomorrodi, T. Pham, F. Z. Bischoff, T. J. Pircher, *J. Oncol.* **2011**, *2011*, 252361.
[25] S. S. Bithi, S. A. Vanapalli, *Sci. Rep.* **2017**, *7*, 41707.
[26] A. F. Sarioglu, N. Aceto, N. Kojic, M. C. Donaldson, M. Zeinali, B. Hamza, A. Engstrom, H. Zhu, T. K. Sundaresan, D. T. Miyamoto, X. Luo, A. Bardia, B. S. Wittner, S. Ramaswamy, T. Shioda, D. T. Ting, S. L. Stott, R. Kapur, S. Maheswaran, D. A. Haber, M. Toner, *Nat. Methods* **2015**, *12*, 685.
[27] M. A. Qasaimeh, S. G. Ricoult, D. Juncker, *Lab Chip* **2013**, *13*, 40.
[28] A. T. Brimmo, M. A. Qasaimeh, *IEEE Nanotechnol. Mag.* **2017**, *11*, 20.
[29] A. T. Brimmo, M. A. Qasaimeh, *RSC Adv.* **2017**, *7*, 5120.
[30] T. A. Yap, D. Lorente, A. Omlin, D. Olmos, J. S. de Bono, *Clin. Cancer Res.* **2014**, *20*, 2553.
[31] D. Juncker, H. Schmid, E. Delamarche, *Nat. Mater.* **2005**, *4*, 622.
[32] M. A. Qasaimeh, M. Pyzik, M. Astolfi, S. M. Vidal, D. Juncker, *Adv. Biosyst.* **2018**, *2*, 1700243.
[33] H. Shiku, T. Yamakawa, Y. Nashimoto, Y. Takahashi, Y. Torisawa, T. Yasukawa, T. Ito-Sasaki, M. Yokoo, H. Abe, H. Kambara, T. Matsue, *Anal. Biochem.* **2009**, *385*, 138.
[34] A. Ainla, E. T. Jansson, N. Stepanyants, O. Orwar, A. Jesorka, *Anal. Chem.* **2010**, *82*, 4529.
[35] A. Brimmo, P. A. Goyette, R. Alnemari, T. Gervais, M. A. Qasaimeh, *Sci. Rep.* **2018**, *8*, 10995.
[36] A. T. Brimmo, A. Menachery, M. A. Qasaimeh, *Lab Chip* **2019**, *19*, 4052.
[37] M. Safavieh, M. A. Qasaimeh, A. Vakil, D. Juncker, T. Gervais, *Sci. Rep.* **2015**, *5*, 11943.
[38] A. D. Stroock, S. K. W. Dertinger, A. Ajdari, I. Mezic, H. A. Stone, G. M. Whitesides, *Science* **2002**, *295*, 647.
[39] G. L. Li, H. He, H. Yan, Q. Zhao, D. Z. Yin, *Clin. Hemorheol. Microcirc.* **2010**, *44*, 145.
[40] A. Martowicz, G. Spizzo, G. Gastl, G. Untergasser, *BMC Cancer* **2012**, *12*, 501.
[41] L. Bai, Y. Du, J. Peng, Y. Liu, Y. Wang, Y. Yang, C. Wang, *J. Mater. Chem. B* **2014**, *2*, 4080.
[42] M. Heine, B. Freund, P. Nielsen, C. Jung, R. Reimer, H. Hohenberg, U. Zangemeister-Wittke, H. J. Wester, G. H. Luers, U. Schumacher, *PLoS One* **2012**, *7*, e36258.
[43] M. Santoni, M. Scarpelli, R. Mazzucchelli, A. Lopez-Beltran, L. Cheng, S. Cascinu, R. Montironi, *J. Biol. Regul. Homeostatic Agents* **2014**, *28*, 555.
[44] M. H. Wang, R. Sun, X. M. Zhou, M. Y. Zhang, J. B. Lu, Y. Yang, L. S. Zeng, X. Z. Yang, L. Shi, R. W. Xiao, H. Y. Wang, S. J. Mai, *Cell Death Dis.* **2018**, *9*, 2.
[45] D. A. Silver, I. Pellicer, W. R. Fair, W. D. W. Heston, C. CordonCardo, *Clin. Cancer Res.* **1997**, *3*, 81.
[46] D. T. Miyamoto, R. J. Lee, S. L. Stott, D. T. Ting, B. S. Wittner, M. Ulman, M. E. Smas, J. B. Lord, B. W. Brannigan, J. Trautwein, N. H. Bander, C. L. Wu, L. V. Sequist, M. R. Smith, S. Ramaswamy, M. Toner, S. Maheswaran, D. A. Haber, *Cancer Discovery* **2012**, *2*, 995.
[47] S. I. Brett, Y. Kim, C. N. Biggs, J. L. Chin, H. S. Leong, *Prostate Cancer Prostatic Dis.* **2015**, *18*, 213.
[48] G. Galletti, L. Portella, S. T. Tagawa, B. J. Kirby, P. Giannakakou, D. M. Nanus, *Mol. Diagn. Ther.* **2014**, *18*, 389.
[49] B. J. Kirby, M. Jodari, M. S. Loftus, G. Gakhar, E. D. Pratt, C. Chanel-Vos, J. P. Gleghorn, S. M. Santana, H. Liu, J. P. Smith, V. N. Navarro, S. T. Tagawa, N. H. Bander, D. M. Nanus, P. Giannakakou, *PLoS One* **2012**, *7*, e35976.
[50] S. M. Santana, H. Liu, N. H. Bander, J. P. Gleghorn, B. J. Kirby, *Biomed. Microdevices* **2012**, *14*, 401.
[51] K. Pantel, S. Riethdorf, *Nat. Rev. Clin. Oncol.* **2009**, *6*, 190.
[52] D. A. Haber, V. E. Velculescu, *Cancer Discovery* **2014**, *4*, 650.
[53] F. H. Karzai, R. A. Madan, W. D. Figg, *South. Med. J.* **2015**, *108*, 224.
[54] Y. P. Hong, F. Fang, Q. Zhang, *Int. J. Oncol.* **2016**, *49*, 2206.
[55] S. Park, R. R. Ang, S. P. Duffy, J. Bazov, K. N. Chi, P. C. Black, H. S. Ma, *PLoS One* **2014**, *9*, e85264.
[56] C. Renier, E. Pao, J. Che, H. E. Liu, C. A. Lemaire, M. Matsumoto, M. Triboulet, S. Srivinas, S. S. Jeffrey, M. Rettig, R. P. Kulkarni, D. Di Carlo, E. Sollier-Christen, *npj Precis. Oncol.* **2017**, *1*, 15.
[57] X. Chen, D. F. Cui, C. C. Liu, H. Li, *Sens. Actuators, B* **2008**, *130*, 216.
[58] N. H. Akhtar, O. Pail, A. Saran, L. Tyrell, S. T. Tagawa, *Adv. Urol.* **2012**, *2012*, 973820.
[59] A. J. Armstrong, M. S. Marengo, S. Oltean, G. Kemeny, R. L. Bitting, J. D. Turnbull, C. I. Herold, P. K. Marcom, D. J. George, M. A. Garcia-Blanco, *Mol. Cancer Res.* **2011**, *9*, 997.
[60] L. K. Liu, K. G. Yang, H. Gao, X. Li, Y. B. Chen, L. H. Zhang, X. J. Peng, Y. K. Zhang, *Anal. Chem.* **2019**, *91*, 2591.
[61] P. Ding, Z. Wang, Z. Wu, W. Zhu, L. Liu, N. Sun, R. Pei, *J. Mater. Chem. B* **2020**, *8*, 3408.
[62] H. J. Yoon, T. H. Kim, Z. Zhang, E. Azizi, T. M. Pham, C. Paoletti, J. Lin, N. Ramnath, M. S. Wicha, D. F. Hayes, D. M. Simeone, S. Nagrath, *Nat. Nanotechnol.* **2013**, *8*, 735.
[63] M. Wilchek, E. A. Bayer, *Methods Enzymol.* **1990**, *184*, 5.

ADVANCED MATERIALS TECHNOLOGIES

Supporting Information

for *Adv. Mater. Technol.,* DOI: 10.1002/admt.202100053

Herringbone Microfluidic Probe for Multiplexed Affinity-Capture of Prostate Circulating Tumor Cells

*Ayoub Glia, Muhammedin Deliorman, Pavithra Sukumar, Farhad K. Janahi, Bisan Samara, Ayoola T. Brimmo, and Mohammad A. Qasaimeh**

WILEY-VCH

Supplementary Information

Herringbone Microfluidic Probe for Multiplexed Affinity-Capture of Prostate Circulating Tumor Cells

*Ayoub Glia, Muhammedin Deliorman†, Pavithra Sukumar†, Farhad K. Janahi, Bisan Samara, Ayoola T. Brimmo, and Mohammad A. Qasaimeh**

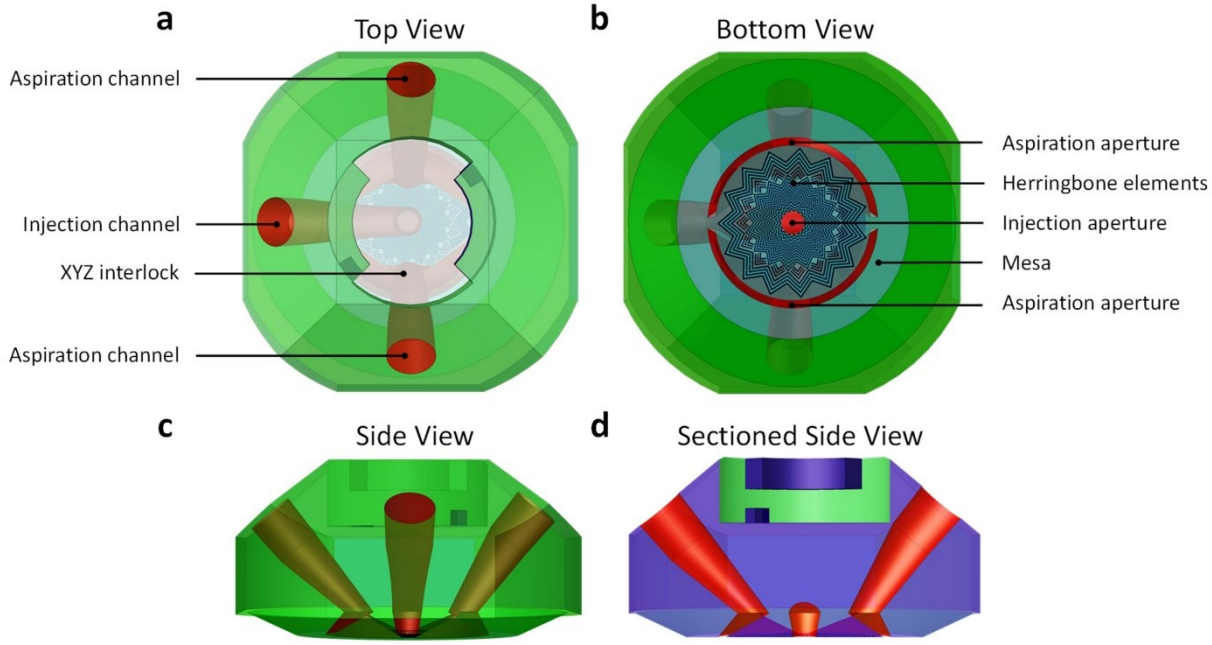

Figure S1. CAD designs of (a) top, (b) bottom, (c) side, and (d) sectioned side view of the HB-MFP. The three fluidic tube channels (two for aspiration and one for injection) are linked to two symmetrical crescent-shaped aspiration peripheral apertures facing each other and one central circular injection aperture in the middle. The interlock mechanism is implemented to connect the HB-MFP to a programmable XYZ micropositioner, so that the device parallel alignment, separation distance, and scanning speed and direction are precisely controlled. The herringbone elements (micromixers) are integrated radially in the mesa region of the HB-MFP for enhanced cell capture efficiency. Drawings are not to scale.

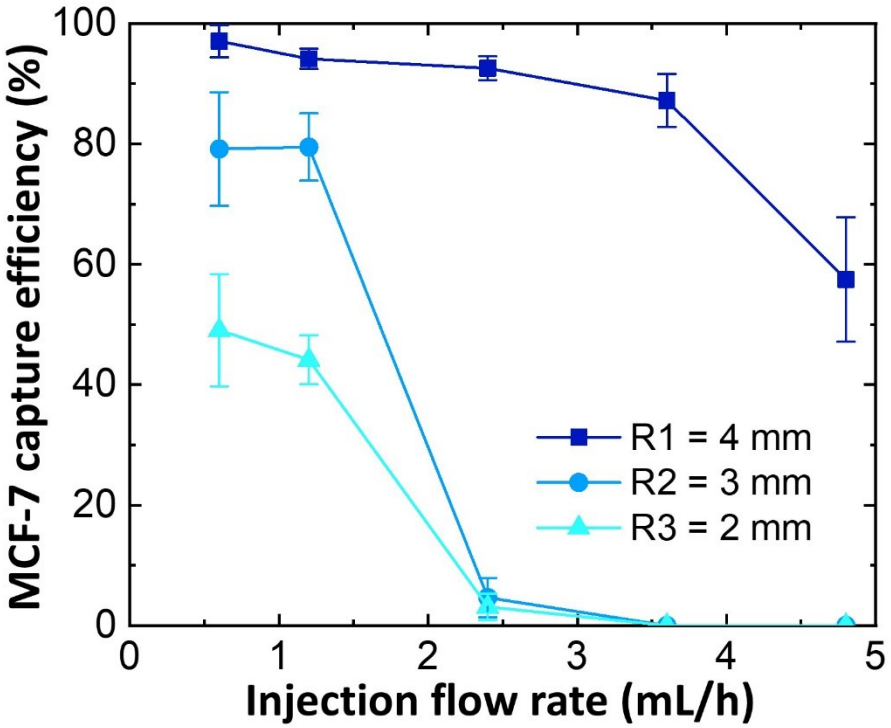

Figure S2. Capture efficiency of MCF-7 cells on anti-EpCAM antibody-activated glass slides at 1.2 mL/h flow rate and using various HB-MFP sizes. Higher capture efficiency is observed with larger R values due to reduced shear stresses. At R = 4 mm the overall capture efficiency is higher because of the lower associated shear stresses and the higher probabilities of cell interaction with the bottom antibodies-coated substrate (larger chaotic path).

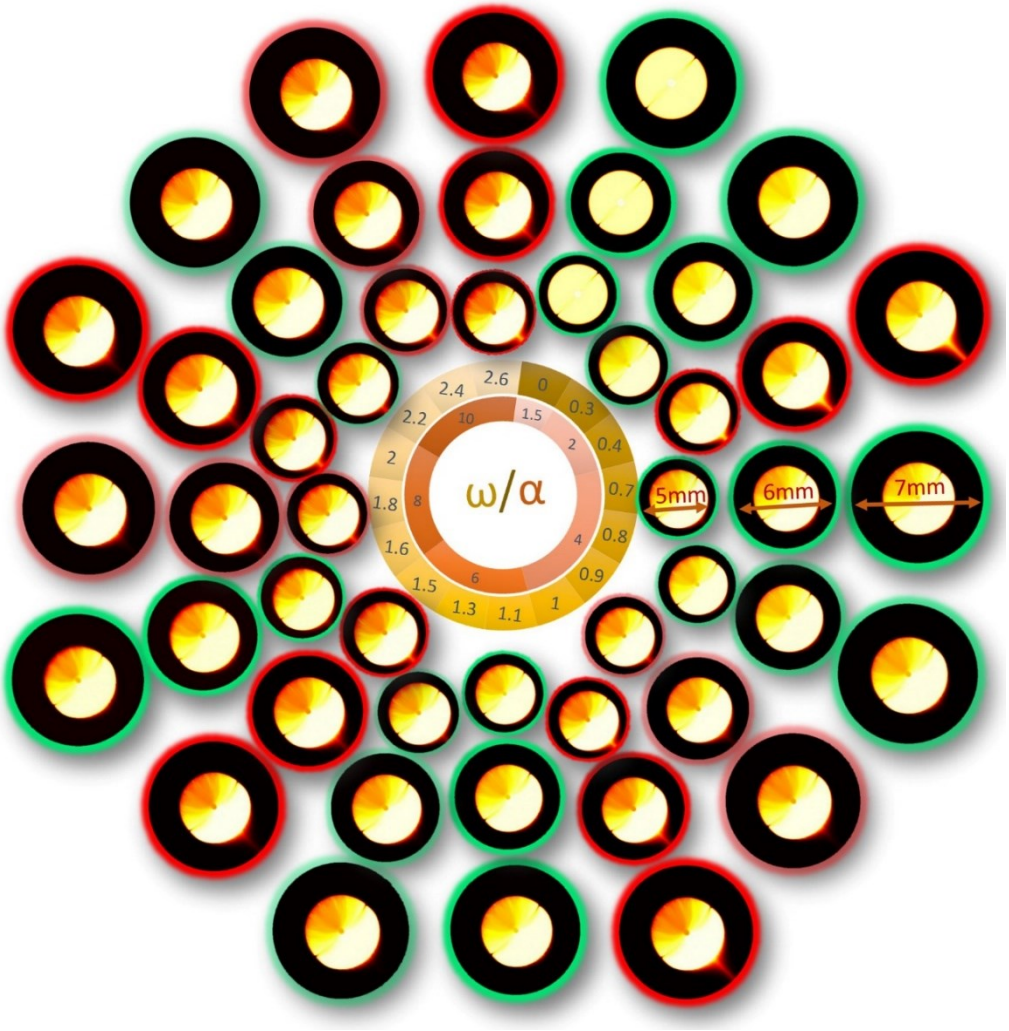

Figure S3. Parametric study of the HB-MFP upon varying ratios of injection/aspiration flow rates (α) and scanning speeds (ω). The results of retained HFC are highlighted in green circular border, whereas the results of leakage are highlighted in red circular boarder.

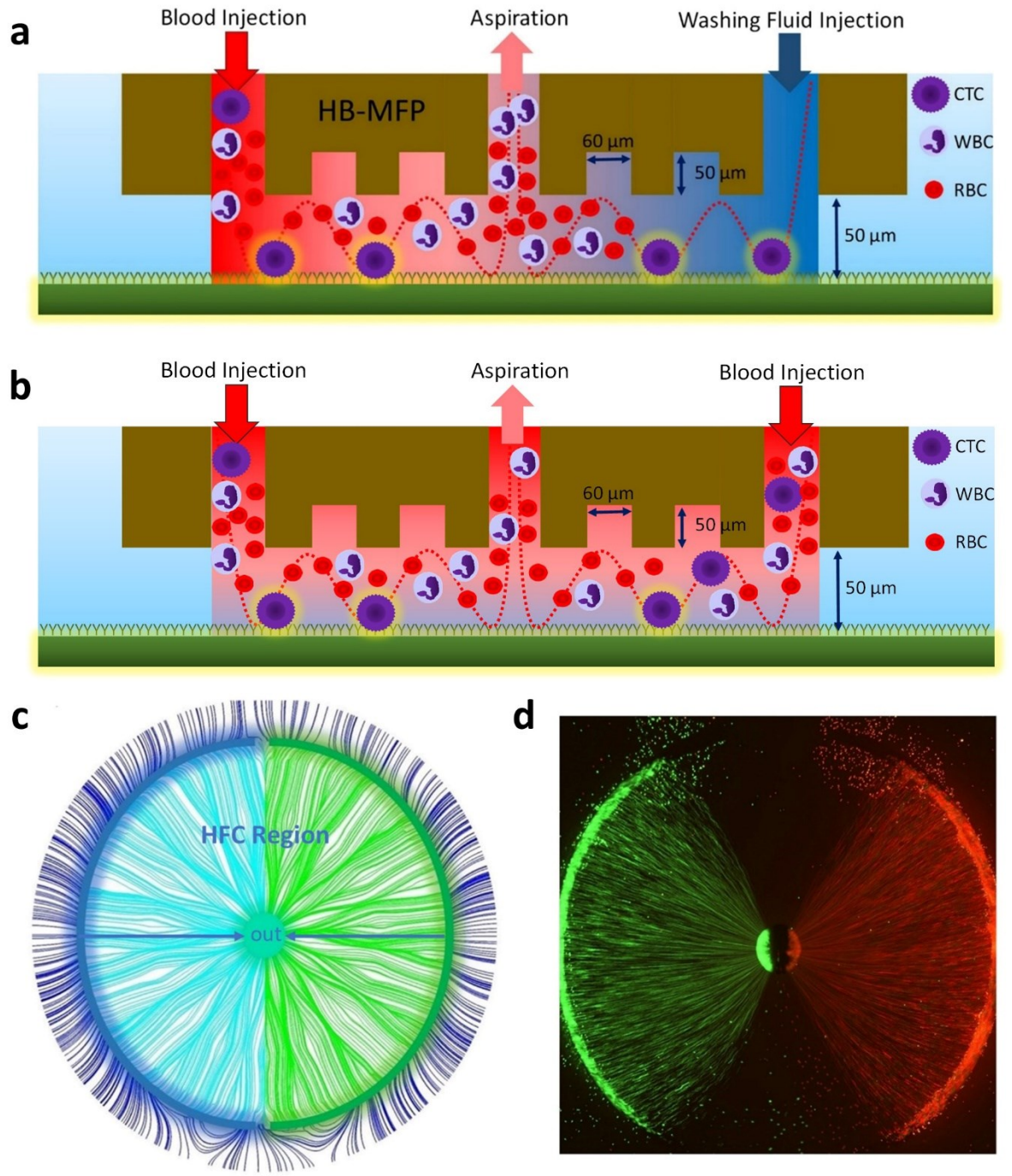

Figure S4. (a) The schematic depicts the HB-MFP in *wash-on-the-fly* mode. In this working concept, the blood is injected from one of the crescent-shaped apertures, while the washing fluid (e.g., PBS) is injected from the other. Both fluids are then aspirated from the central aperture. (b) The schematic of the HB-MFP depicts another configuration, where the blood is injected from both crescent-shaped apertures and is aspirated from the central aperture. This configuration requires higher aspiration to injection flow rate ratio to maintain the HFC. (c) The plot of velocity streamlines (generated from a 3D finite element) shows the HFC region and the chaotic mixing induced by the HB elements. The blue arrows represent the direction of the fluid when it is injected from the crescent-shaped apertures and aspirated at the central aspiration aperture. (d) Fluorescence image shows the motion of red and green fluorescent microbeads when injected from the crescent-shaped apertures, revealing the HFC within the plane of processing area. Note that, with this setup ~33% of the processing area is not effective due to the high values of α.

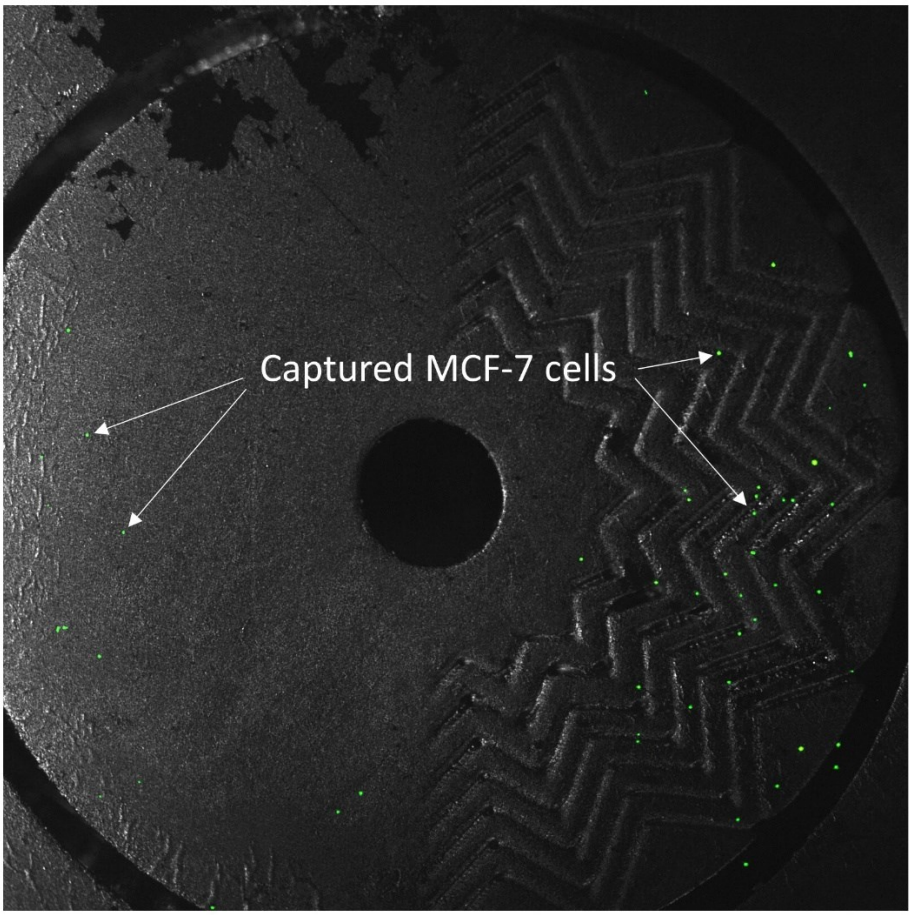

Figure S5. The effect of HB-MFP herringbone elements on the capture efficiency of MCF-7 cells on the functionalized bottom substrate. The cell capture is significantly higher in the regions below the herringbone elements as compared to those below the flat mesa (no herringbone elements).

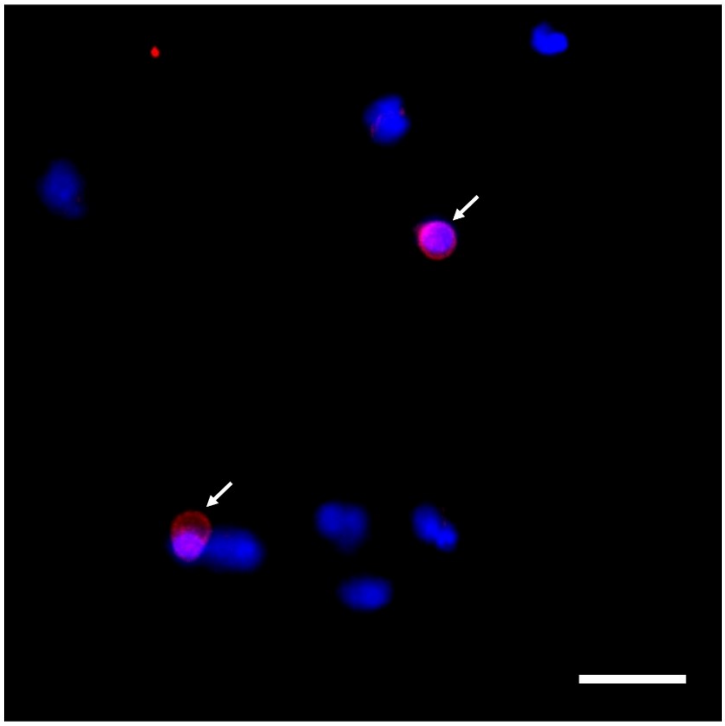

Figure S6. Fluorescent images of captured CTCs and WBCs revealed the immunostaining of their nuclei (blue, DAPI+ for CTCs and WBCs) and CD45 (red, CD45+ for WBCs, white arrows). Scale bar is 30 μm.

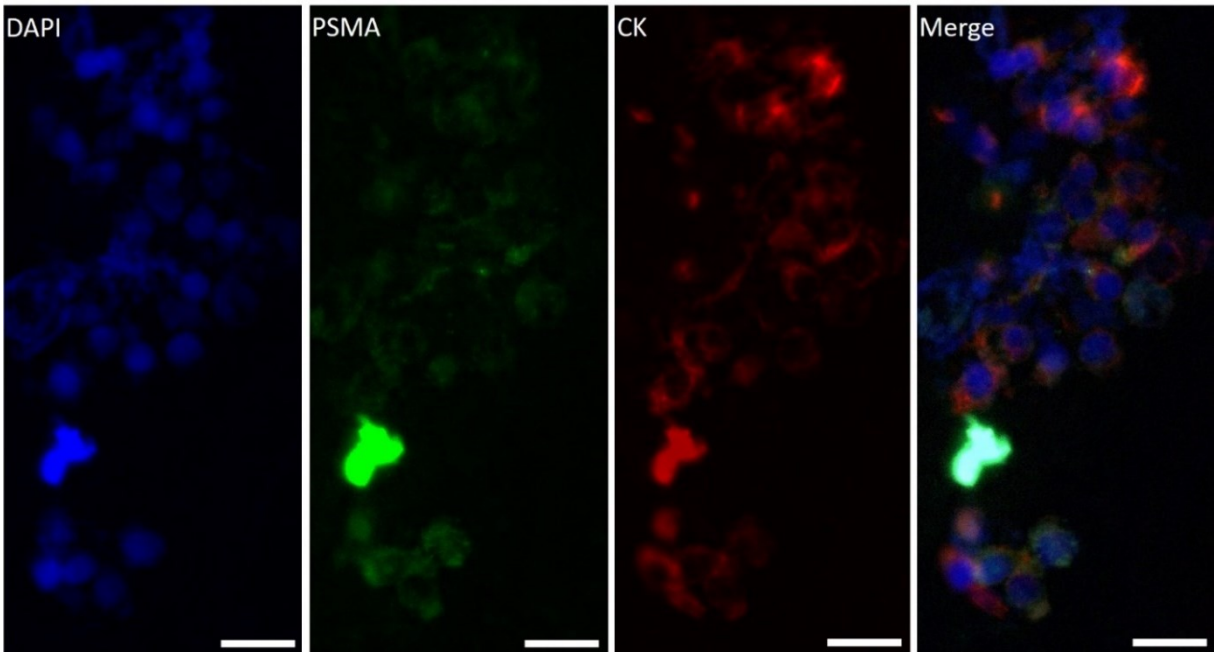

Figure S7. Fluorescent images of a captured CTC cluster, which showed positive to immunostaining of their nucleus (blue, DAPI+), PSMA (green, PSMA+), and cytoplasmic cytokeratin (red, CK+). Scale bars are 30 μm.